INTERFACIAL VIBRATIONAL CHEMISTRY OF I. MIXED SURFACTANT SYSTEMS II. ALKYL HALIDE UPTAKE AND ATMOSPHERIC IMPLICATIONS

A Thesis

Presented in Partial Fulfillment of the Requirements for

the Degree Master of Science

in the Graduate School of The Ohio State University

By

Kandice L. Harper, B.S.

*****

The Ohio State University
2007

Master's Examination Committee:

Professor Heather C. Allen, Adviser

Professor James F. Rathman

Approved by

_____

Adviser
Graduate Program in Chemistry

ABSTRACT

As interfaces between various phases of matter are ubiquitous in the environment, the chemistry that occurs at these interfaces is of great interest and importance. In these studies, vibrational sum frequency generation (VSFG) spectroscopy is used to selectively probe the interfacial molecules of atmospherically relevant model systems. Pure and mixed fatty acid and phospholipid monolayers at the air-aqueous interface are used as a model for the fat-coat found on the surface of some naturally occurring atmospheric aerosols. Phase segregation is observed in a 1:1 mixture of oleic and palmitic acids, and the oleic acid molecules are observed to influence the structure of the palmitic acid molecules that are in close association. In addition, the soluble surfactant sodium dodecyl sulfate, a model for more hydrophilic surfactants found in the aqueous aerosol core, is observed to compete with the molecules of an insoluble lipid film for surface sites at the air-aqueous interface. Increased conformational ordering of the acyl chains of the lipid molecules is observed in the mixed system. The results of these studies indicate that the molecular composition of both the aerosol surface and the aqueous core can affect the surface structure of the aerosol, which has the potential to affect the processing of the aerosol in the atmosphere. Additionally, the adsorption and uptake of gas-phase alkyl halide and alcohol molecules by aqueous surfaces are studied due to their potential to

participate in atmospheric interfacial chemistry. Although the alcohols studied are observed at the air-aqueous interface, a convolution of residence time, number density, and orientation prevent the alkyl halide molecules from being detected at the aqueous surface with VSFG. Nonetheless, bulk phase analysis using Raman spectroscopy indicates that methyl chloride is taken up into the bulk aqueous phase from the gas phase.

Dedicated to Kyle and my family

ACKNOWLEDGMENTS

A great number of people have helped me to accomplish this task, and I am grateful to all of them. I especially thank my adviser, Dr. Heather Allen, for all of the support, knowledge, and encouragement provided to me during my time at The Ohio State University. I am thankful for the professional opportunities that she has provided for me to be successful. I am also indebted to Dr. Laura Voss, Dr. Gang Ma, and (Dr.) Lisa Van Loon for sharing their knowledge of all things in and out of the laboratory. Without their assistance, the experiments presented in this thesis would not have been realized. I also acknowledge Dr. Laura Voss for her contributions to the manuscript that we submitted for publication in co-authorship, of which a modified version is presented in Chapter 3 of this thesis. I am grateful to all members of the Allen Lab and friends in the department for providing an endlessly amusing place to work! I thank all of my family members for their ceaseless support. I especially thank Kyle Poorman for all of the support and optimism that he provided for the duration of this process. Finally, I acknowledge the National Science Foundation for funding the research presented in this thesis.

VITA

23 April 1981 ..... Born - New Hartford, Iowa

2002-2003 ..... Undergraduate Researcher
Houk Research Group-Iowa State University

May 2003 ..... B.S. Chemistry
Iowa State University

2003-2004 ..... Intern
Hach Chemical

2001-2004 ..... Wetlands and Watershed Laboratory Researcher
Crumpton Research Group-Iowa State University

2004-2007 ..... Graduate Teaching Assistant
The Ohio State University

2004-2007 ..... Graduate Research Assistant
Allen Research Group-The Ohio State University

FIELDS OF STUDY

Major Field: Chemistry

TABLE OF CONTENTS

LIST OF FIGURES

LIST OF ABBREVIATIONS

DMPC	1,2-dimyristoyl-*sn*-glycero-3-phosphocholine
DOPC	1,2-dioleoyl-*sn*-glycero-3-phosphocholine
DPPC	1,2-dipalmitoyl-*sn*-glycero-3-phosphocholine
POPC	1-palmitoyl-2-oleoyl-*sn*-glycero-3-phosphocholine
Å	Angstrom
A.U.	arbitrary units
AS	asymmetric stretch
BBSFG	broad bandwidth sum frequency generation
cm	centimeter
CCD	charge-coupled device
ºC	degrees Celsius
fs	femtosecond
FR	Fermi resonance
g/mm	grooves per millimeter
IR	infrared
I.D.	inner diameter
MΩ	Megaohms
MeOH	methyl alcohol
MeCl	methyl chloride

μm	micrometer
nm	nanometer
BuOH	n-butyl alcohol
BuBr	n-butyl bromide
BuCl	n-butyl chloride
OA	oleic acid
O.D.	outer diameter
PA	palmitic acid
ps	picosecond
SDS	sodium dodecyl sulfate
sccm	standard cubic centimeter per minute
SFG	sum frequency generation
SS	symmetric stretch
VSFG	vibrational sum frequency generation
VIS	visible
W	Watt
cm^{-1}	wavenumber

CHAPTER 1

INTRODUCTION

Heterogeneous chemical processes have been recognized to play important roles in the chemistry of our atmosphere.[1] Interfacial chemistry is especially important in the atmosphere due to the abundance of surfaces available for interaction with gas-phase molecules, including the surfaces of aerosols (biogenic and anthropogenic), the open ocean, fog and rain droplets, and the quasi-liquid layer of ice. Despite the importance of such processes and the abundance of surfaces available to support their occurrence, atmospheric processes that occur at the interface between two phases are generally less well characterized than those that occur in a single phase.

The importance of heterogeneous atmospheric processes has been demonstrated previously.[1] For example, evidence exists for the formation of a surface complex ($OH\ldots Cl^-$) during the production of gas-phase molecular chlorine from interfacial aqueous Cl^- and gas-phase OH.[2] In this case, single-phase reactions alone were unable to account for the experimentally observed production of molecular chlorine, and inclusion of the interfacial processes was necessary to make the model predictions consistent with the experimental observations.

Without doubt, single-phase chemical reactions are extremely important in describing atmospheric processes. However, such reactions cannot adequately account for all of the chemistry in our atmosphere, and important heterogeneous reactions must also be taken into account. In practice, accounting for interfacial chemistry can prove to be a challenging task due to the complex nature of most naturally occurring surfaces in contact with the atmosphere.

For example, insoluble long-chain hydrocarbons with polar headgroups form films at the surface of aqueous aerosols in an inverse micelle configuration, in which the polar headgroups associate with the aqueous subphase and the non-polar hydrocarbon tails are oriented toward the gaseous atmosphere.[3,4] Such surfactant films may have important effects on atmospheric processes, such as the uptake of species from the atmosphere and the evaporation of water from the aqueous aerosol core.[3-10] The molecules that comprise these films have a wide variety of sizes and physical conformations, and the interactions between the molecules residing at the interface will play a large role in how these films interact with their environment and how the aerosols are processed in the atmosphere. Thus, a fundamental understanding of the structure of the molecules residing at such interfaces is a critical first step in understanding the physical and chemical phenomena that occur there.

Characterizing the interactions between the molecules residing at an interface is as important as characterizing the interactions between the interfacial and bulk phase molecules as the bulk phase molecules move into the interface. Thus, the studies presented in this thesis are investigations of model systems of atmospherically relevant

interfaces. The experiments presented in Chapter 3 probe the structure and interactions of surfactant molecules residing at the air-aqueous interface as a fundamental study to understand the surfaces of fat-coated aerosols. The experiments presented in Chapter 4 probe the interactions of interfacial surfactants with a soluble surfactant introduced to the bulk aqueous phase. Finally, the experiments presented in Chapter 5 probe the interactions of gas-phase molecules with the aqueous surface as the gas-phase molecules are taken up into the aqueous bulk phase. The spectroscopic technique of vibrational sum frequency generation (VSFG) spectroscopy, described in detail in Chapter 2, is used to selectively study the molecules at the air-aqueous interfaces in the following investigations.

CHAPTER 2

VIBRATIONAL SUM FREQUENCY GENERATION

2.1 Vibrational Sum Frequency Generation Theory

Detailed theoretical descriptions of the sum frequency process are available in the literature.[11-15] Only a brief description of this spectroscopic technique is presented here. Vibrational sum frequency generation (VSFG) is a second-order nonlinear optical technique that provides vibrational spectra of interfacial molecules. In VSFG, a coherent sum frequency beam is generated by spatially and temporally overlapping a visible beam with an infrared beam at a sample surface. The resulting sum frequency beam has a frequency, ω_{SFG}, that is the sum of the frequencies of the two incident beams, ω_{VIS} and ω_{IR} (equation 2.1).

$$\omega_{SFG} = \omega_{VIS} + \omega_{IR} \tag{2.1}$$

Both reflected and transmitted sum frequency beams are generated. Conservation of momentum and phase matching considerations dictate that the reflected sum frequency beam occurs at the angle predicted by equation 2.2.

$$n_{SF} k_{SF} \sin\theta_{SF} = n_{VIS} k_{VIS} \sin\theta_{VIS} \pm n_{IR} k_{IR} \sin\theta_{IR} \tag{2.2}$$

In this equation, n is the index of refraction of the medium through which the indicated beam travels, k is the wave vector of the beam and is equal to ω/c (ω is the relevant frequency and c is the speed of light in vacuum), and θ is the angle of the indicated beam to the surface normal. The addition sign is appropriate for experimental geometries utilizing co-propagating visible and infrared beams, whereas the subtraction sign is appropriate for counter-propagating beam geometries.

The detected sum frequency signal originates from the molecules residing at the interface between two isotropic bulk phases and provides molecular-level structural information of these molecules. Polarization analysis of the sum frequency signal aids in spectral interpretation. Being an optical technique, VSFG can be used for a wide range of pressures and is useful for investigations of liquid samples that often cannot be studied using high vacuum surface science techniques. The following experiments are investigations of the air-liquid interface, and, therefore, provide vibrational spectra of molecules adsorbed to liquid surfaces at atmospheric pressure.

The intensity of the sum frequency signal is shown in equation 2.3.

$$I^{\omega_{SFG}}(\omega) \propto \left| E^{\omega_{SFG}} \cdot \chi^{(2)} : E^{\omega_{VIS}} E^{\omega_{IR}} \right|^2 I^{\omega_{VIS}} I^{\omega_{IR}} \tag{2.3}$$

$I^{\omega_{SFG}}$, $I^{\omega_{VIS}}$, and $I^{\omega_{IR}}$ are the intensities of the exigent sum frequency, incident visible, and incident infrared beams, respectively, $\chi^{(2)}$ is the macroscopic second-order nonlinear susceptibility tensor for the interfacial molecules, and the absolute square term is the electric field at the interface, where the indicated E terms include Fresnel factors that describe the relationship between the induced nonlinear polarization of the interface and

both the incoming beams and the generated sum frequency beam. Detailed mathematical representations of the Fresnel factors can be found in the literature.[11,14-16]

$\chi^{(2)}$ is comprised of a nonresonant term and a sum of resonant terms (equation 2.4).

$$\left|\chi^{(2)}\right|^2 = \left|\chi^{(2)}_{NR} + \sum_v \chi^{(2)}_v\right|^2 \tag{2.4}$$

The general description of a single resonant component of $\chi^{(2)}$ corresponding to the v vibrational mode is presented in equation 2.5.

$$\chi^{(2)}_v \propto \frac{A_v}{\omega_{IR} - \omega_v + i\Gamma_v} \tag{2.5}$$

A_v is the strength of the sum frequency transition moment of the v vibrational mode and includes both the Raman and infrared transition moments of the vibration, ω_v is the center frequency of the transition, and Γ is the natural line-width of the transition. When the frequency of the incident infrared beam approaches the frequency of the vibrational transition, $\omega_{IR} - \omega_v$ approaches zero and the value of $\chi^{(2)}_v$ increases, resulting in an increase in the intensity of the sum frequency signal (refer to equation 2.3). Figure 2.1 shows the energy level diagram for the sum frequency process, which is considered to be anti-Stokes Raman scattering off of a vibrationally excited state. VSFG provides vibrational spectra that are up-shifted into the visible region of the spectrum by the sum frequency process, providing a clear experimental advantage over other vibrational spectroscopies that require the use of less sensitive infrared detection schemes.

$\chi_v^{(2)}$ is a third-rank tensor with 27 individual elements. Thus, to be rigorously accurate in notation, the resonant components must be denoted as $\chi_{IJK,v}^{(2)}$, where I, J, and K each represent a Cartesian coordinate (x, y, or z) in the laboratory reference frame. Equation 2.6 shows the relationship between the sum frequency signal (via $\chi_{IJK,v}^{(2)}$) and both the number density and the orientation of the interfacial molecules.

$$\chi_{IJK,v}^{(2)} = N\langle\beta_{IJK,v}\rangle \tag{2.6}$$

N represents the number density of the surface species, $\beta_{IJK,v}$ represents the molecular hyperpolarizability for the v vibrational mode in the laboratory reference frame, and $\langle\ldots\rangle$ represents an average over the orientational distribution of the molecules. The orientation angle of a molecule from the surface normal can be determined experimentally, and one method for this calculation is discussed in detail in Chapter 4. An Euler angle transformation, denoted $\mu_{IJK:lmn}$ in equation 2.7, is used to convert between the laboratory reference frame and the molecular reference frame (denoted by the subscripts l, m, and n).

$$\beta_{IJK,v} = \sum_{lmn} \mu_{IJK:lmn}\beta_{lmn,v} \tag{2.7}$$

The mathematical representation of the molecular hyperpolarizability in the molecular reference frame (equation 2.8) explicitly illustrates the selection rules for the sum frequency process.

$$\beta_{lmn,v} = \frac{\langle g|\alpha_{lm}|v\rangle\langle v|\mu_n|g\rangle}{\omega_{IR} - \omega_v + i\Gamma_v} \tag{2.8}$$

In this representation, $\langle g|\alpha_{lm}|v\rangle$ is the Raman transition moment, and $\langle v|\mu_n|g\rangle$ is the infrared transition moment, where g is the ground vibrational state and ν is the excited

vibrational state. The molecular hyperpolarizability is nonzero only when the Raman and infrared transition moments are nonzero. Thus, a vibrational mode must be both Raman and infrared active in order for the vibration to be sum frequency active.

In addition to these selection rules, a lack of inversion symmetry is required for VSFG to be allowed, which is the basis for the interface selectivity of VSFG. An investigation of the Raman and infrared transition moments elucidates this final selection rule for VSFG activity.[17] The electric dipole moment is a vector with three components, μ_x, μ_y, and μ_z (equation 2.9).

$$\mu = \begin{bmatrix} \mu_x \\ \mu_y \\ \mu_z \end{bmatrix} \tag{2.9}$$

Each component corresponds to one of the three Cartesian coordinates (in the molecular reference frame) and has the same symmetry as the corresponding translation (x, y, or z). A vibration is infrared active if any of the components of the dipole moment change during the vibration. The polarizability of a molecule is a second-rank tensor with nine components and is a measure of the ability of an applied electric field to induce an electric dipole moment in the molecule. An applied electric field along a given axis can induce a dipole having any of the components μ_x, μ_y, and μ_z (equation 2.10).

$$\begin{bmatrix} \mu_x \\ \mu_y \\ \mu_z \end{bmatrix} = \begin{bmatrix} \alpha_{xx} & \alpha_{xy} & \alpha_{xz} \\ \alpha_{yx} & \alpha_{yy} & \alpha_{yz} \\ \alpha_{zx} & \alpha_{zy} & \alpha_{zz} \end{bmatrix} \begin{bmatrix} E_x \\ E_y \\ E_z \end{bmatrix} \tag{2.10}$$

Thus, a field applied along the x-axis can induce a dipole along the x-, y-, and z-axes. In equation 2.10, μ_r corresponds to the dipole moment induced along the r–axis and E_r

corresponds to an applied electric field along the r–axis. The polarizability tensor is symmetric with the result that $\alpha_{xy} = \alpha_{yx}$, $\alpha_{xz} = \alpha_{zx}$, and $\alpha_{yz} = \alpha_{zy}$. The six unique components of the polarizability tensor, α_{xx}, α_{xy}, α_{xz}, α_{yy}, α_{yz}, and α_{zz}, have the symmetries xx, xy, xz, yy, yz, and zz (or a linear combination of these). A vibration is Raman active if any of the components of the polarizability change during the vibration.

Because the components of μ have the same symmetry as the translations x, y, and z, they have odd parity under inversion (i.e., they change sign under inversion). However, the components of α transform as quadratics and have even parity since they are equivalent before and after inversion. Because a vibrational state cannot simultaneously have odd and even parity, a lack of inversion symmetry is necessary for a vibration to be simultaneously infrared and Raman active and, therefore, sum frequency active. This requirement must also be satisfied macroscopically because $\chi^{(2)}_{IJK,v}$ is a macroscopic orientational average of the molecular hyperpolarizabilities (equation 2.6).

Macroscopically, the requirement is fulfilled at interfaces between two isotropic bulk phases. Sum frequency generation is forbidden in bulk phases where the molecules experience a centrosymmetric environment. The molecules residing at the interface between these two isotropic bulk phases experience a non-centrosymmetric environment and are sum frequency active by this selection rule. The unique requirement for both Raman and infrared activity, in combination with the requirement for a lack of inversion symmetry, is the basis for the interface-specificity of VSFG.

Symmetry constraints reduce the number of non-zero components of $\chi^{(2)}_{IJK,v}$ to only seven: $\chi^{(2)}_{zxx,v}$, $\chi^{(2)}_{zyy,v}$, $\chi^{(2)}_{xzx,v}$, $\chi^{(2)}_{yzy,v}$, $\chi^{(2)}_{xxz,v}$, $\chi^{(2)}_{yyz,v}$, and $\chi^{(2)}_{zzz,v}$. Only non-zero components

can contribute to the sum frequency signal and are determined by defining the z-axis to be parallel to the surface normal and by assuming that the surface plane (i.e., the x-y plane) is isotropic. Complete details of the symmetry restrictions at the surface can be found elsewhere.[14,15] Because the x- and y-axes are equivalent for an isotropic surface, $\chi^{(2)}_{zxx,v} \equiv \chi^{(2)}_{zyy,v}$, $\chi^{(2)}_{xzx,v} \equiv \chi^{(2)}_{yzy,v}$, and $\chi^{(2)}_{xxz,v} \equiv \chi^{(2)}_{yyz,v}$. The four unique components of the macroscopic susceptibility are probed experimentally by using different polarization combinations of the three beams (listed in the order: SFG, VIS, IR). The electric field is perpendicular to the plane of incidence (the plane containing the surface normal and the incident beams) for S-polarized light and is parallel to the plane of incidence for P-polarized light. When the x-axis is in the incident plane, S-polarized light has only a y-component in the laboratory reference frame, and P-polarized light has both x- and z-components, as shown in Figure 2.2. Thus, $\chi^{(2)}_{yyz,v}$ is probed by SSP polarization combination (S-polarized SFG, S-polarized VIS, P-polarized IR), $\chi^{(2)}_{yzy,v}$ is probed by SPS polarization combination (S-polarized SFG, P-polarized VIS, S-polarized IR), $\chi^{(2)}_{zyy,v}$ is probed by PSS polarization combination (P-polarized SFG, S-polarized VIS, S-polarized IR), and $\chi^{(2)}_{xxz,v}$, $\chi^{(2)}_{xzx,v}$, $\chi^{(2)}_{zxx,v}$, and $\chi^{(2)}_{zzz,v}$ are probed by PPP polarization combination (P-polarized SFG, P-polarized VIS, P-polarized IR). The first two subscripts of $\chi^{(2)}_{IJK,v}$ are interchangeable because they refer to the Raman process. Thus, $\chi^{(2)}_{yzy,v}$ and $\chi^{(2)}_{zyy,v}$ are equivalent, and SPS and PSS polarization combinations provide similar spectra (the only difference is in the associated Fresnel factors). Experimentally, only SSP, SPS, and PPP polarization combinations are used in the following studies.

2.2 Broad Bandwidth Sum Frequency Generation Instrumentation

Complete descriptions of the broad bandwidth sum frequency generation (BBSFG) spectrometer employed in the following experiments can be found elsewhere.[18] A brief description is provided here, and a diagram of the instrument is shown in Figure 2.3. The BBSFG system uses two regenerative amplifiers (Spectra-Physics Spitfire, femtosecond and picosecond versions) to produce fs and ps visible pulsed laser beams with 1 kHz repetition rates. Each regenerative amplifier is seeded by half of the output from a mode-locked Ti:Sapphire laser (Spectra-Physics Tsunami) and is pumped by a Q-switched all solid-state Nd:YLF laser (Spectra-Physics Evolution-30). The Ti:Sapphire oscillator has an output centered at 800 nm with a bandwidth of approximately 350 cm^{-1} (82 MHz repetition rate, sub-50 fs pulse duration) and is pumped by 4.7 W of power from a diode-pumped continuous wave Nd:YVO_4 laser (Spectra-Physics Millennia Vs). The 1064 nm output from the lasing transition in the Millennia Vs is frequency doubled to 532 nm using an intra-cavity LBO crystal. The Evolution-30 laser is also intra-cavity frequency doubled using an LBO crystal, resulting in 20 W of 527 nm output (1 kHz repetition rate) that is used to pump the Ti:Sapphire rods in the femtosecond (8 W) and picosecond (12 W) regenerative amplifiers.

The regenerative amplifiers produce pulses of high peak power (1 kHz repetition rate) by stretching the seed pulses from the Tsunami by positive chirping, amplifying the stretched pulses in the resonator cavity, and then compressing the amplified pulses upon cavity dumping. The output of the picosecond regenerative amplifier is a narrow bandwidth visible beam (800 nm center wavelength, 15 cm^{-1} bandwidth, 2 ps pulse

duration)[18] that is used for the sum frequency process. The output of the femtosecond regenerative amplifier is a broad bandwidth visible beam (800 nm center wavelength, ~300 cm^{-1} bandwidth, 85 fs pulse duration)[18] that is used in an optical parametric amplifier (Spectra-Physics OPA-800CF) to generate the broad bandwidth infrared pulses that are used for sum frequency generation. In the OPA, nonlinear processes in a β-barium borate (BBO) crystal produce signal and idler beams that subsequently undergo difference frequency mixing in a $AgGaS_2$ crystal to produce a broad bandwidth infrared beam. The wavelength of the infrared output is selected by angle tuning the BBO crystal. The spectral bandwidth of the infrared beam is >300 cm^{-1} in both the C-H and C-D stretching regions probed in these experiments.

Mirrors direct the picosecond visible and femtosecond infrared beams through polarization optics and focusing lenses to the sample surface where they are spatially and temporally overlapped. The infrared beam is focused onto the sample surface using a bi-convex BaF_2 lens (125 mm focal length at 4μm), and a MgF_2 window is used for polarization selection. The visible beam is focused slightly beyond the sample surface using a 500 mm focal length lens to prevent the sample from being damaged by the high power at the focal point. A half-wave plate is used in combination with a Glan polarizer in the visible beam line for power attenuation, and a second half-wave plate is used for polarization selection. Temporal overlap of the beams at the sample surface is achieved by adjusting a delay stage in the visible beam line. Spatial and temporal overlap of the narrow bandwidth picosecond visible and broad bandwidth femtosecond infrared beams generates the broad bandwidth sum frequency beam (>300 cm^{-1} in both C-H and C-D

stretching regions). This broad bandwidth technique generates a full vibrational spectrum from each laser pulse. Because large signal-to-noise ratios can be achieved in seconds, dynamic surface processes can be monitored with this instrument, such as the phase transitions during the compression of lipid monolayers at the air-water interface.

A co-propagating geometry is used for the visible and infrared beams, and the reflected sum frequency beam is detected (Figure 2.4). The angles of the infrared, visible, and sum frequency beams from the surface normal are 71°, 58°, and 60°, respectively. The reflected visible beam is spatially filtered after the sample, and all residual light is optically filtered by three short pass (SPF-750, CVI, Albuquerque, NM) and two notch (Kaiser Optical Systems, Inc., Ann Arbor, MI) filters positioned in the sum frequency beam line. The reflected sum frequency beam subsequently passes through a Glan polarizer, used for polarization selection, and a 75 mm focal length lens that focuses the beam onto the slit of a 500 mm monochromator (Acton Research, SpectraPro SP-500). The sum frequency beam is dispersed by a 1200 g/mm grating blazed at 750 nm in the monochromator and then detected by a liquid nitrogen-cooled CCD (Roper Scientific, LN 400EB, back-illuminated, 1340 x 400 pixel array). The monochromator is controlled using SpectraSense software (Acton Research, version 4.4.0) and is calibrated using the 435.83 nm peak of fluorescent light. The resolution of the BBSFG system is approximately 8 cm^{-1}. [19]

Sum frequency peak positions are calibrated in the C-H stretching region using the absorption bands of a polystyrene film positioned in the infrared beam line during acquisition of a sum frequency spectrum of a GaAs crystal. In the C-D stretching region,

sum frequency peak positions are calibrated using the absorption bands of ambient CO_2 vapor. Background spectra are acquired for each sample by adjusting the delay stage in the visible line to disrupt the temporal overlap of the beams, and the background-subtracted sum frequency spectra are normalized to the nonresonant signal from a GaAs crystal surface. Igor software (Wavemetrics, Inc., version 3.1) is used to plot and fit the sum frequency data. The sum frequency spectra presented in this thesis are plots of the sum frequency intensity versus the incident infrared frequency.

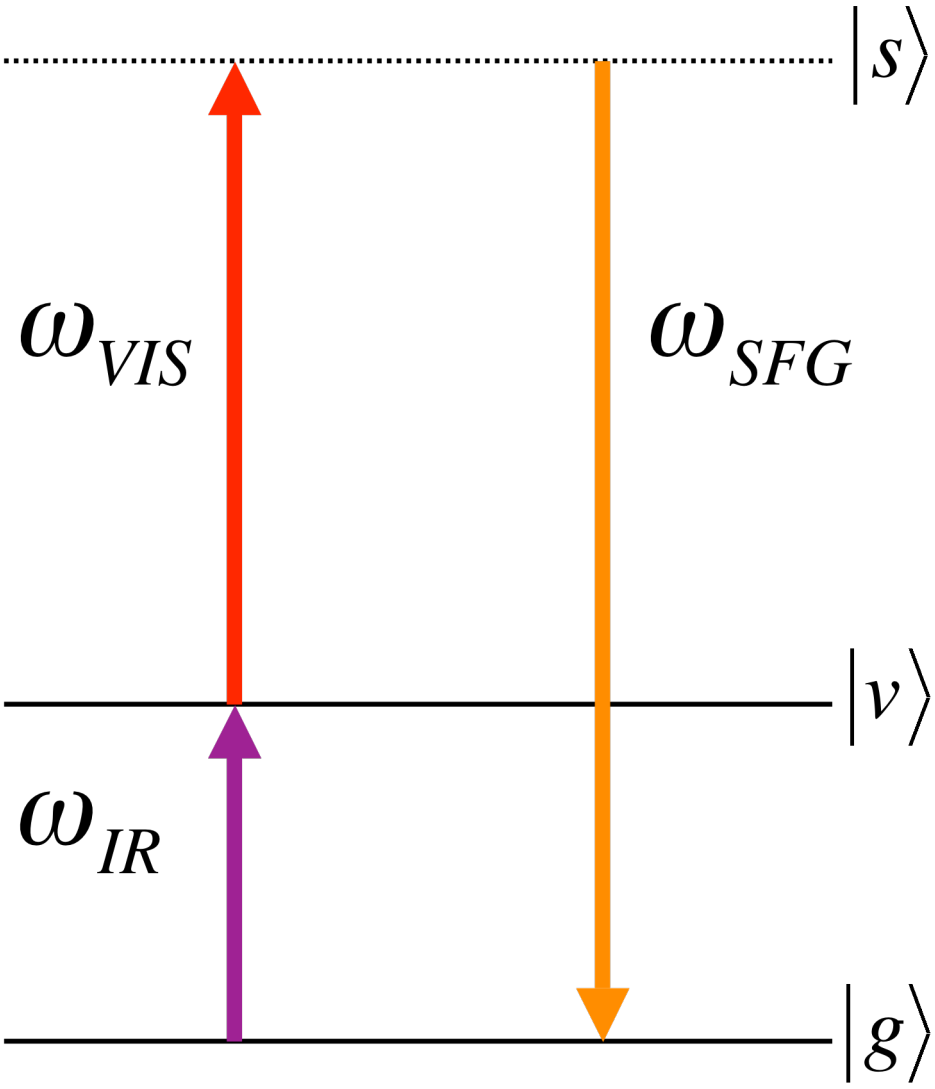

Figure 2.1. Energy level diagram for the sum frequency process. $|g\rangle$ is the ground state, $|v\rangle$ is a vibrationally excited state, and $|s\rangle$ is a virtual state that is far from an electronic state of the molecule.

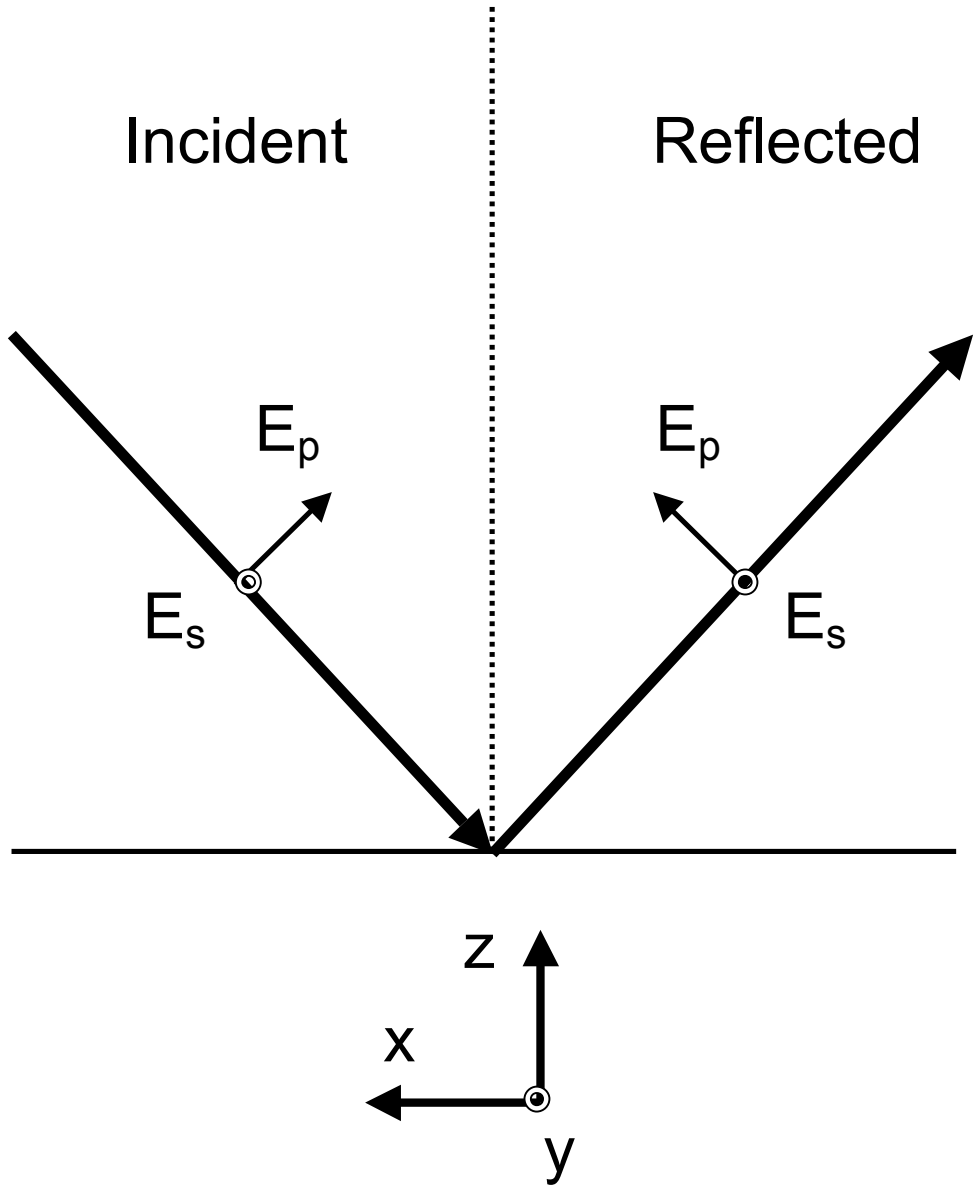

Figure 2.2. S- and P- polarized electric field vectors for incident and reflected beams. S-polarized light has only a y-component when the plane of incidence is the x-z plane, shown here as the plane of the page. P-polarized light has both x- and z-components in this reference frame.

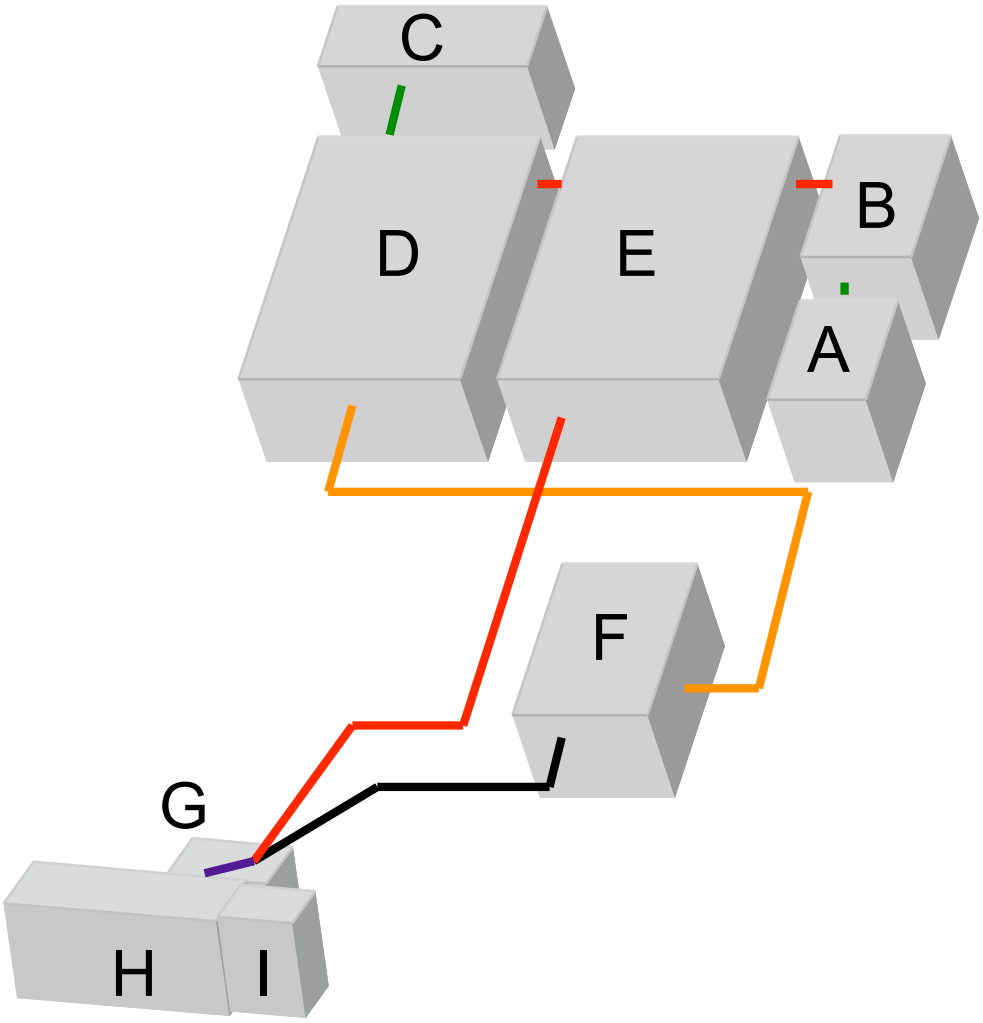

Figure 2.3. Broad bandwidth sum frequency generation system: (a) Nd:YVO_4 laser, (b) Ti:Sapphire laser, (c) Nd:YLF laser, (d) femtosecond regenerative amplifier, (e) picosecond regenerative amplifier, (f) optical parametric amplifier, (g) sample stage, (h) monochromator, and (i) CCD. Beam paths shown are representations only and correspond to: orange-fs visible, red-ps visible, black-fs infrared, and purple-sum frequency.

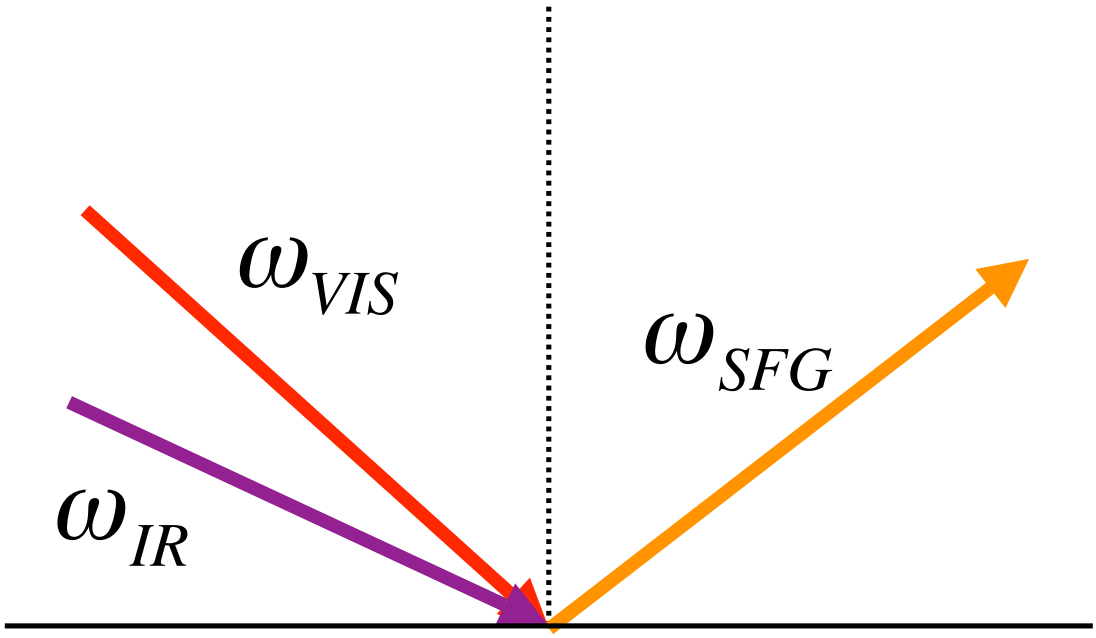

Figure 2.4. Co-propagating beam geometry used for sum frequency experiments. Spatial and temporal overlap of the visible (red) and infrared (purple) beams at the sample surface is necessary for generation of the sum frequency beam (orange). The reflected sum frequency beam is detected in these experiments.

CHAPTER 3

PURE AND MIXED FATTY ACID AND PHOSPHOLIPID MONOLAYERS

For several years, it has been recognized that organic surfactant-like molecules may play an important role in the chemistry of atmospheric aerosols.[3,4,20] These surfactant species are long-chain hydrocarbons attached to various functional groups, including sulfates, phosphates, alcohols, and carboxylic acids, among others. The naturally occurring fat coat found on the surfaces of atmospheric aerosols is believed to play a major role in the processing of these aerosols in the atmosphere.[3,4,9,20] Because of the wide variety of organic surfactants that are believed to exist in atmospheric aerosols, a fundamental understanding of the structures and interactions of various surfactant species at aqueous surfaces is necessary to understand the processing of such aerosols in the atmosphere.

In the experiments presented here, a Langmuir trough is coupled with the VSFG system to obtain both spectroscopic and thermodynamic data of pure and mixed insoluble monolayers at the air-water interface during isothermal compression. Pure and mixed fatty acid systems are compared with the corresponding phosphocholine. Noting their prevalence in naturally occurring atmospheric aerosols,[21-23] fatty acids and

phosphocholines with palmitoyl and oleoyl chains are studied. The palmitoyl chain is a fully saturated C_{16} acyl chain, and the oleoyl chain is a singly unsaturated C_{18} acyl chain with a *cis* double bond between carbons 9 and 10, as depicted in the top panel of Figure 3.1. The R-groups on the acyl chains are either a single hydrogen atom, making the species a fatty acid, or one of the positions on a phosphocholine headgroup, also shown in Figure 3.1. The R-groups attached to the phosphocholine headgroup can be either the same acyl chain or two different chains, resulting in an asymmetric phosphocholine. Studies of the mixed acyl chains both as fatty acids (palmitic and oleic acids) and as the acyl chains attached to a single phosphocholine headgroup (1-palmitoyl-2-oleoyl-*sn*-glycero-3-phosphocholine), as shown in Figure 3.1, are presented. Pure monolayers of the fatty acids and the corresponding symmetric phosphocholines are also studied.

3.1 Materials

Solutions of oleic acid (OA), palmitic acid (PA), palmitic acid with a deuterated acyl chain (PA-d31), 1,2-dioleoyl-*sn*-glycero-3-phosphocholine (DOPC), 1,2-dipalmitoyl-*sn*-glycero-3-phosphocholine with deuterated acyl chains (DPPC-d62), and 1-palmitoyl-2-oleoyl-*sn*-glycero-3-phosphocholine with a deuterated palmitoyl chain (POPC-d31) were prepared in chloroform (99.8%, Sigma-Aldrich). Oleic acid (99%) was obtained from Sigma-Aldrich, palmitic acid (99%) was obtained from Aldrich, and palmitic acid-d31 (98%) was obtained from Cambridge Isotope Laboratories, Inc. (Andover, MA). DOPC (99%), DPPC-d62 (98%), and POPC-d31 (98%) were obtained from Avanti Polar Lipids, Inc. (Alabaster, AL). All chemicals were used as received. Structures of these species are depicted in Figure 3.1. Solutions of 1:1 oleic acid:palmitic

acid-d31 and of 1:1 palmitic acid:palmitic acid-d31 were prepared from the fatty acid solutions. Monolayers were spread on deionized water with a resistivity of 18.3 MΩ-cm (Barnstead Nanopure).

3.2 Experimental Method

In this study, the optical parametric amplifier was tuned so that the infrared light was centered at either 2900 cm^{-1} to cover the C-H stretching region of the acyl chain of oleic acid or 2100 cm^{-1} to cover the C-D stretching region of the deuterated acyl chain of palmitic acid and had a spectral bandwidth of ~400 cm^{-1} in both of these regions. Taking advantage of the different vibrational frequencies of deuterated acyl chains from their protiated counterparts allows the study of mixed monolayer systems. In this study, the palmitoyl acyl chains probed are deuterated, and the oleoyl acyl chains probed are protiated.

The input energy to the sample surface was 300 μJ/pulse from the visible beam and 8 μJ/pulse from the infrared beam. BBSFG data reported in this work were recorded in the SSP polarization combination (S-polarized SFG, S-polarized visible, P-polarized infrared). All spectra are background-subtracted and normalized to the nonresonant VSFG signal produced from a GaAs crystal. Peak frequencies are reported as the observed frequencies, not from spectral fits.

Surface pressure-area isotherms were obtained with a low-volume Langmuir trough (KSV Instruments Limited Minitrough) equipped with two Delrin barriers used to symmetrically compress the film. The surface pressure was monitored during film compression using a Wilhelmy plate made of filter paper. The aqueous subphase was

replaced after each experiment. A measured volume of lipid solution was spread on deionized water with the barriers in the open position using a 50-μL Hamilton syringe. Ten minutes elapsed before isothermal compression to allow the chloroform solvent to evaporate. The barriers were compressed at a rate of 5 mm/minute. Isothermal compression data for the pure and mixed monolayers are depicted in Figure 3.2. BBSFG spectra, averaged for 30 seconds of data acquisition, were taken concurrently with isotherm compression data. All experiments were conducted at room temperature (23°C) and at atmospheric pressure. All isotherms were obtained at least 3 times to ensure reproducibility. The Langmuir trough was placed in a box, which was continuously purged with nitrogen, in order to inhibit the oxidation of the oleoyl chains with ambient ozone.[24]

3.3 Results and Discussion

In this study, the Langmuir trough was coupled with the BBSFG experiment to take concurrent thermodynamic and spectroscopic data of the monolayer. The isotherms shown in Figure 3.2 are typical for the lipids studied.[25] Data were collected to the point just before film collapse. The data have been normalized by plotting the isotherms as the surface pressure versus the mean area per chain, since the phosphocholine species have two acyl chains per molecule and the fatty acids have only one. The top panel of Figure 3.2 is isothermal compression data of a PA-d31 monolayer. Phase transitions occur as the PA-d31 monolayer transitions from the gas-condensed coexistence region to the tilted condensed phase at mean chain area of 25 $Å^2$ and then from the tilted condensed phase to the untilted condensed phase at a mean chain area of 18 $Å^2$, as is consistent with

previously published palmitic acid isotherms.[26] The second isotherm in Figure 3.2 is the isotherm for DPPC-d62, the corresponding phosphocholine to PA-d31. This phosphocholine is comprised of two palmitoyl chains attached to a single phosphocholine headgroup, as pictured in Figure 3.1. The differences between the isotherms of the fatty acid and the phosphocholine show the difference in the phase behavior of the materials, where the DPPC-d62 monolayer is in the gas-liquid coexistence region before undergoing a first-order phase transition at 47 $Å^2$/chain. The monolayer is then in the liquid expanded phase before entering the liquid expanded-tilted condensed coexistence region at 31 $Å^2$/chain and then finally undergoing another first-order phase transition to the tilted condensed phase at 24 $Å^2$/chain. The differences in the phase behavior are attributed to the effects of the headgroup, since the acyl chains of the fatty acid and phosphocholine are identical. The phosphocholine headgroup also allows the monolayer to be compressed to a higher surface pressure before film collapse, as evidenced in the isothermal compression data.

BBSFG data was taken concurrently with the isothermal compressions. The isotherms for the PA-d31 and DPPC-d62 are replotted in Figures 3.3 and 3.4, respectively. The spectra demonstrate how this surface-specific technique can be used to monitor phase changes in the monolayers. The labels correspond to the points in the isotherm where the spectra were taken. Both Figures 3.3a and 3.4a are spectra taken after the lipid was spread but before compression of the barriers began. At this point, the acyl chains in the monolayer are both dispersed and disordered and, therefore, not satisfying the requirements for number density or overall orientation for a detectable VSFG signal.

As the monolayers are compressed, the number density in the spot where the beams are overlapped increases. More importantly, however, is that as the monolayers undergo phase transitions, the overall order in the monolayer changes, meeting the requirement for net orientation of the acyl chains. An increase in the number density and the orientation leads to an increase in the VSFG signal from the monolayer. The peaks in the VSFG spectra in these figures are attributed to the CD_3 symmetric stretch (SS; 2066 cm^{-1}), the CD_2 SS (2096 cm^{-1}), the CD_3 Fermi resonance (FR; 2121 cm^{-1}), the CD_2 asymmetric stretch (AS; 2198 cm^{-1}), and the CD_3 AS (2217 cm^{-1}), following assignments made by Yang et al.[27] In the final frame for each of the figures (3.3c and 3.4e), the SSP-polarization VSFG peaks from the CD_2 SS and CD_2AS are absent, indicating that the acyl chains are free of gauche defects with CD_2 vibrational signals being canceled through inversion symmetry.[28,29] The CD_2 peaks are, however, evident in the spectra of the monolayers when in less ordered states. The presence of these peaks in Figures 3.3b, 3.4b, and 3.4c is evidence of gauche defects in the acyl chains.[29]

The OA isotherm presented in the third panel of Figure 3.2 is also consistent with previously published isotherms and shows the liquid-gas coexistence region above the first-order phase transition at 51 $Å^2$/chain, the liquid phase region from 28 to 51 $Å^2$/chain, and the film-collapse occurring at 28 $Å^2$/chain.[25,30] VSFG spectra are presented in Figure 3.5 with the peaks present in the OA monolayer spectra attributed to the CH_2 SS (2846 cm^{-1}), the CH_3 SS (2876 cm^{-1}), the CH_2 FR (2923 cm^{-1}), the CH_3 FR (2941 cm^{-1}), and the olefinic (=CH) stretch at the carbon-carbon double bond (3014 cm^{-1}), following assignments and arguments made by Wang and co-workers.[31] The isothermal

compression data and BBSFG data are also consistent with previously published results from the Allen group,[24] where the intensity of the CH_3 SS is the highest intensity peak when the monolayer is in the most ordered, fully compressed state.

The fourth panel of Figure 3.2 is the isotherm for DOPC, the corresponding phosphocholine to OA with two oleoyl chains attached to a single headgroup. As in the OA isotherm, the DOPC isotherm shows a single phase transition from the gas-liquid coexistence region to the liquid phase at 59 $Å^2$/chain. This phase transition is shifted to the right on the isotherm compared to the OA isotherm, once again indicating that the difference in the headgroup is affecting the phase behavior of the monolayer. Figure 3.6 is the concurrent isothermal compression and BBSFG data for the DOPC monolayer. The increase in VSFG intensity between 2925 and 2975 cm^{-1} is attributed to the C-H stretching from the phosphocholine head group, as demonstrated in the VSFG spectra of the C-H stretching region for a DPPC-d62 monolayer presented in Figure 3.7. In this spectrum, the C-D stretching from the acyl chains is not present due to the difference in frequency of the C-D stretching region from the C-H stretching region, and the signal comes solely from the protiated headgroup. The peaks present are the CH_2 SS at 2912 cm^{-1}, the CH_2 AS at 2950 cm^{-1}, and the choline (N-CH_3) SS occurring at 2974 cm^{-1}. [32] The difference in the peak intensity ratio between the CH_3 SS and CH_2 SS from the acyl chain in the fully compressed OA monolayer compared to the DOPC monolayer indicates that the oleoyl chains in the DOPC monolayer are in a more disordered state than those in the OA monolayer.[24] Both the isotherm and the spectroscopic data show how changing the

headgroup from a carboxylic acid to a phosphocholine affects the orientation of the monolayer at the air-water interface.

Lipid monolayers occurring in natural systems are not the pure systems represented by the data presented thus far. Instead, naturally occurring monolayers are comprised of mixtures of lipids. The final two panels of Figure 3.2 are of monolayers with a mixture of acyl chains. The penultimate isotherm in Figure 3.2 is for a 1:1 OA:PA-d31 mixture. This isotherm, when compared to the pure fatty acid monolayers, demonstrates colligative properties of the mixture. The lift-off point where the surface pressure begins to read a value above zero is shifted to a lower mean chain area compared to the pure OA monolayer. The surface pressure sustainable before collapse by the mixed monolayer is higher than the pure OA monolayer and lower than the PA-d31 monolayer. The corresponding phosphocholine to the 1:1 OA:PA-d31 mixture is POPC-d31, a phosphocholine with one protiated oleoyl chain and one deuterated palmitoyl chain attached to the same headgroup. The isothermal compression data for this species is presented in the final panel of Figure 3.2. Again, the initial phase transition from the gas-liquid coexistence region occurs at a lower mean chain area in the phosphocholine than in the fatty acid system, and the ultimate achievable surface pressure is higher for the phosphocholine system than for the corresponding fatty acid system.

Following theory and arguments presented by Goodrich,[25,33] the isothermal compression data is used to determine whether or not the 1:1 OA:PA-d31 monolayer is phase separated by calculating the excess Gibbs energy of mixing,

$$G^E(\pi) = \int_0^{\pi} A^E d\pi \tag{3.1}$$

where the excess area, A^E, for the binary mixture is calculated by

$$A^E = A_{12} - x_1 A_1 - x_2 A_2 , \tag{3.2}$$

and A_{12}, A_1, and A_2 are the mean molecular areas of the mixed monolayer and the pure monolayers at the given surface pressure, π. A^E and $G^E(\pi)$ for the 1:1 OA:PA-d31 monolayer at surface pressures of 5, 10, 15, 20, 25, and 30 mN/m are plotted in Figure 3.8. The positive excess areas and excess Gibbs free energies at all surface pressures indicate that the OA and PA-d31 in the monolayer are phase separated.

The contribution to the VSFG signal from the different acyl chains in the mixed monolayer systems can be determined by taking advantage of the different vibrational frequencies of C-H and C-D stretching modes. The VSFG spectra of the 1:1 OA:PA-d31 and POPC-d31 monolayers taken in both the C-D and C-H stretching regions, showing the contribution from the deuterated palmitoyl and protiated oleoyl chains respectively, are shown in Figures 3.9 and 3.10. The experimental setup does not allow simultaneous acquisition of the spectra in both regions. Therefore, the C-D spectra shown in Figures 3.9 and 3.10 are from different, but reproducible, isothermal compressions than those in the C-H stretching region. As with the previously presented lipids, peaks in the VSFG spectra for the 1:1 OA:PA-d31 mixture and POPC-d31 are not evident until after the first-order phase transition from the coexistence region to a more ordered phase.

The decrease in BBSFG signal in the spectra of monolayers with mixed acyl chains compared to the monolayers with only one acyl species is attributed to the decrease in both number density and orientational order of the monolayer at the interface. To better understand the structure of the acyl chains in the monolayers, experiments were

designed to increase the signal-to-noise ratio. Monolayers were compressed in the Langmuir trough to the point just before film collapse and then the surface pressure was maintained through computer control of the barriers to take spectra using a 2-minute acquisition. Spectra taken in this manner are presented in Figures 3.11, 3.12, and 3.13. Figure 3.11 shows the C-D stretching region for the monolayers with deuterated acyl chains, including the spectra of a 1:1 PA(protiated):PA-d31 monolayer. The spectrum of this mixture demonstrates the effect of a change in number density at the interface on the BBSFG signal. Figure 3.12 shows the C-H stretching region for the monolayers with protiated acyl chains. Figure 3.13 shows the mixed acyl chain monolayers from Figures 3.11 and 3.12 replotted on a different scale to make changes in BBSFG intensity more evident.

Focusing first on the differences in the C-D stretching region, the absence of CD_2 stretching in the PA-d31 and POPC-d31 monolayers presented in Figure 3.11 indicates that the palmitoyl chains in these monolayers are free from gauche defects. The CD_2 peaks are also absent in the spectrum of the 1:1 PA(protiated):PA-d31 monolayer presented in both Figures 3.11 and 3.13. The change in VSFG intensity between this spectrum and the PA-d31 monolayer spectrum is solely attributed to the change in the number of deuterated acyl chains in the probe area. The CD_2 stretching peaks are, however, present in the spectra of the monolayers of mixed oleoyl and palmitoyl chains (1:1 OA:PA-31 and POPC-d31), indicating that there are some gauche defects in the palmitoyl chains in these monolayers. The *cis* configuration of the double bond for the oleoyl chains disrupts the packing of the palmitoyl chains, making an all-*trans*

conformation energetically unfavorable. Comparing the CD_3 SS peak intensity of the 1:1 PA(protiated):PA-d31 monolayer to that of the 1:1 OA:PA-d31 and the POPC-d31 monolayers shows how the change in order leads to a significant change in the VSFG intensity in this peak, since the total number of deuterated palmitoyl chains in all three monolayers is the same. The signal intensity from the CD_3 SS is strongest when the methyl group is oriented perpendicular to the water surface and decreases as the methyl group becomes more parallel to the surface.[31] The decrease in the signal indicates that the terminal methyl group is oriented more parallel to the surface when gauche defects are present in the palmitoyl chain.

Comparing the spectra of the two monolayers comprised of mixed oleoyl and palmitoyl chains confirms the conclusion from the isothermal compression data that the OA and PA-d31 are not miscible and that phase separation is occurring. The spectra of POPC-d31 shows what a fully miscible 1:1 OA:PA-d31 spectra would look like, since the phosphocholine headgroup connects the acyl chains and forces the two units into a complete mixed configuration. In the C-D stretching region in Figure 3.13, the intensity of the CD_2 peaks is weaker and that of the CD_3 SS peak is stronger in the 1:1 OA:PA-d31 mixture than in the *P*OPC-d31 monolayer indicating that, overall, the palmitoyl chains in the 1:1 OA:PA-d31 monolayer have fewer gauche defects and are more well aligned. This indicates that there are islands of PA-d31 in the 1:1 OA:PA-d31 mixture. The evidence of gauche defects in the spectrum from this monolayer indicates, however, that the OA is disrupting the packing of the PA-d31. The palmitoyl chains around the edge of

the aggregates would have gauche defects due to their close proximity to the surrounding oleoyl chains.

Furthermore, when comparing the spectrum of the POPC-d31 monolayer to the 1:1 OA:PA-d31 monolayer in the C-H stretching region in Figures 3.12 and 3.13, OA aggregation is evidenced. As stated above, order in the OA monolayer can be deduced from the ratio of the intensities of the CH_3 and the CH_2 symmetric stretches. In the 1:1 OA:PA-d31 monolayer, not only is the overall intensity higher but the ratio of the CH_3 SS:CH_2 SS intensity is also higher. Both of these phenomena are indicators of more order in the protiated acyl chains and of OA aggregation.

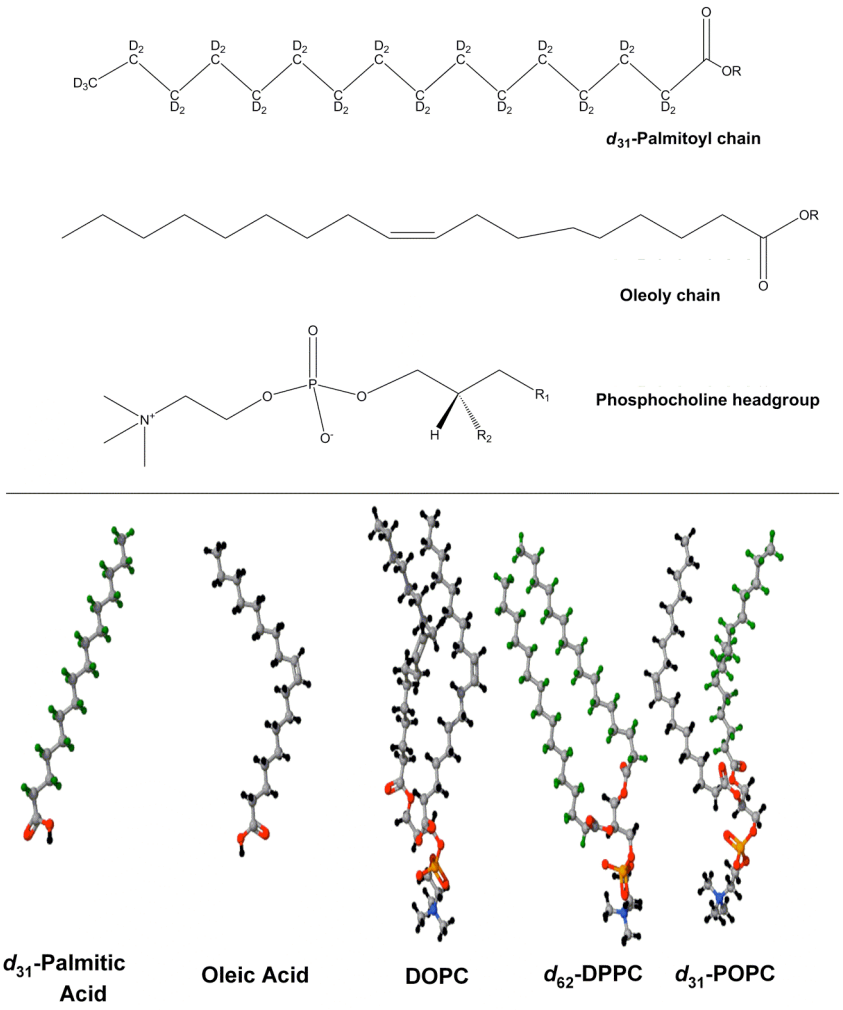

Figure 3.1. Schematics of lipids used in study. Deuterated acyl chains are represented with green deuteriums.

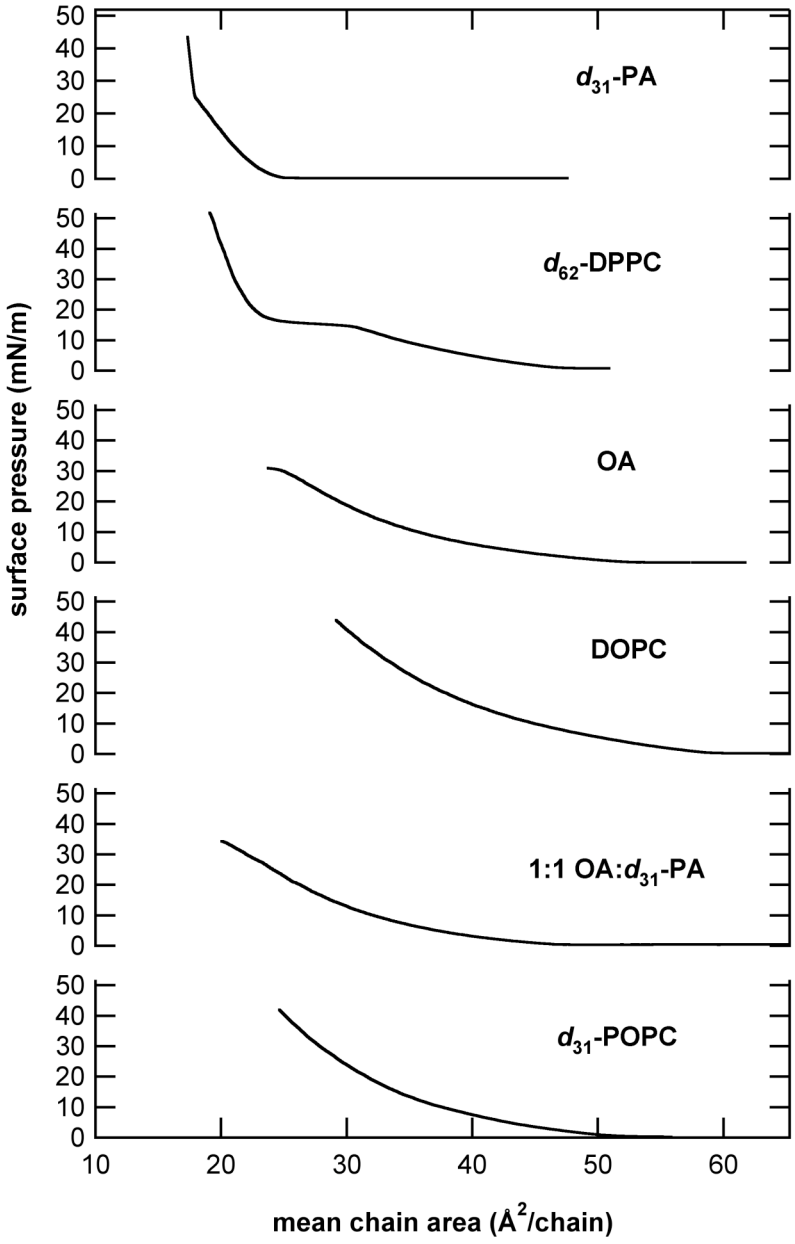

Figure 3.2. Isothermal compression data. Data are taken to the point just before film collapse and are normalized by plotting the surface pressure versus mean area per acyl chain.

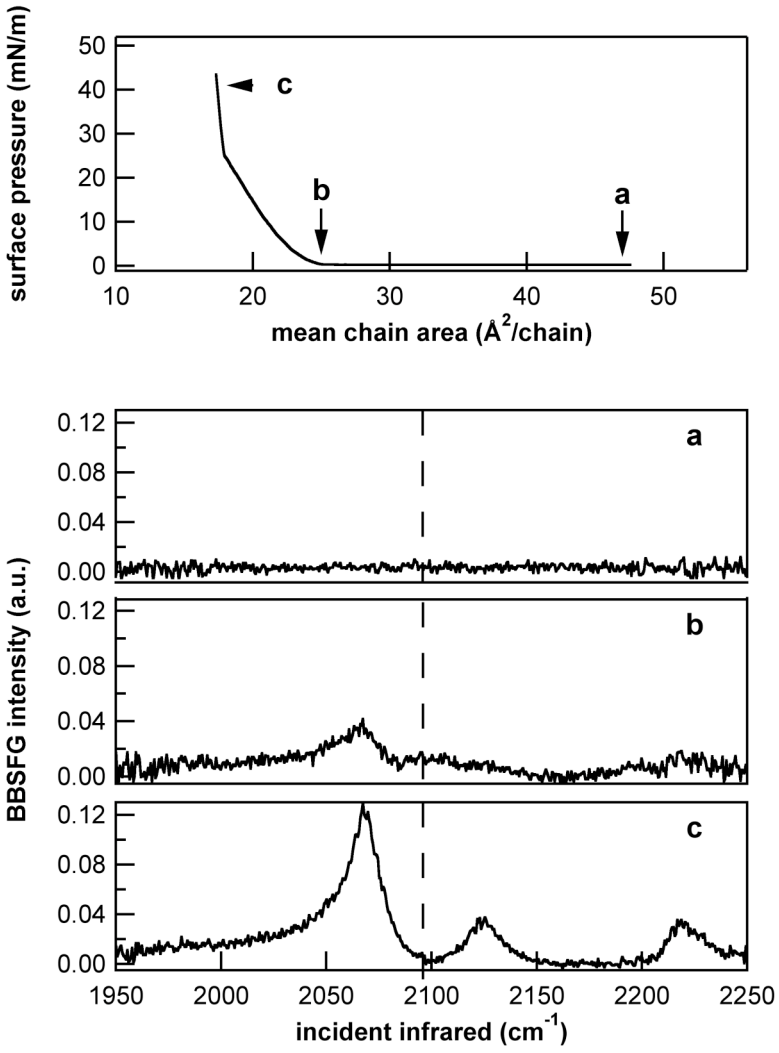

Figure 3.3. Concurrent Langmuir compression isotherm data and BBSFG spectra of a d_{31}-palmitic acid monolayer at the air-water interface. The top graph is the Langmuir isotherm with markers indicating where BBSFG spectra are taken: (a) before beginning compression, (b) just after the first-order phase transition from the gas-condensed phase coexistence region evident at 25 Å^2/chain, and (c) after the phase transition from the tilted condensed phase to the untilted condensed phase and just before the film collapses at 18 Å^2/chain. The peaks in the BBSFG spectra are the CD_3 SS (2066 cm^{-1}), the CD_2 SS (2096 cm^{-1}), the CD_3 FR (2121 cm^{-1}), the CD_2 AS (2198 cm^{-1}), and the CD_3 AS (2217 cm^{-1}). Spectral acquisition times were 30 seconds. The dashed line at 2096 cm^{-1} is a guide to the eye marking the CD_2 SS.

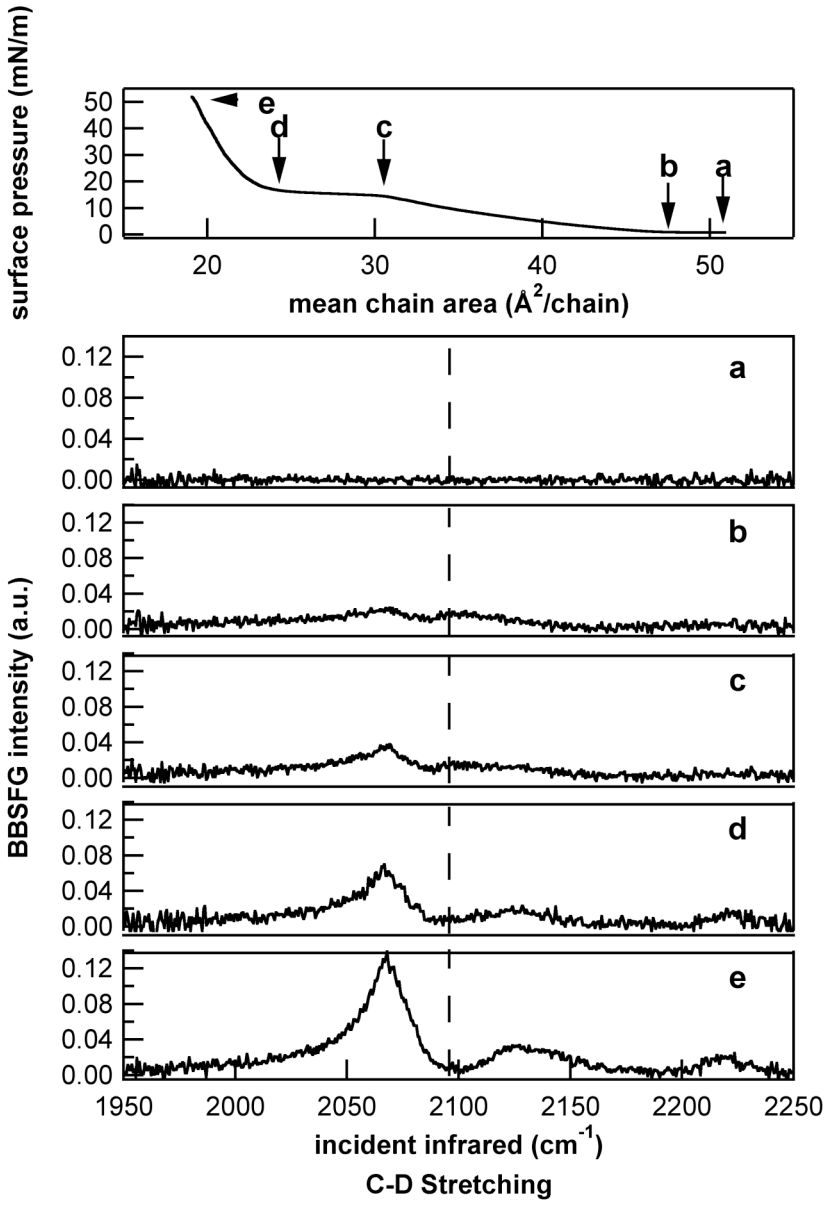

Figure 3.4. Concurrent Langmuir compression isotherm data and BBSFG spectra of a d_{62}-DPPC monolayer at the air-water interface. The top graph is the Langmuir isotherm with markers indicating where BBSFG spectra are taken: (a) before beginning compression, (b) just after the first-order phase transition from the gas-liquid coexistence region evident at 47 Å^2/chain, (c) at the beginning of the liquid expanded-tilted condensed coexistence region at 31 Å^2/chain, (d) just after the first-order phase transition from the liquid expanded-tilted condensed coexistence region to the titled condensed phase at 24 Å^2/chain, and (e) just before film collapse. The dashed line at 2096 cm^{-1} is a guide to the eye marking the CD_2 SS.

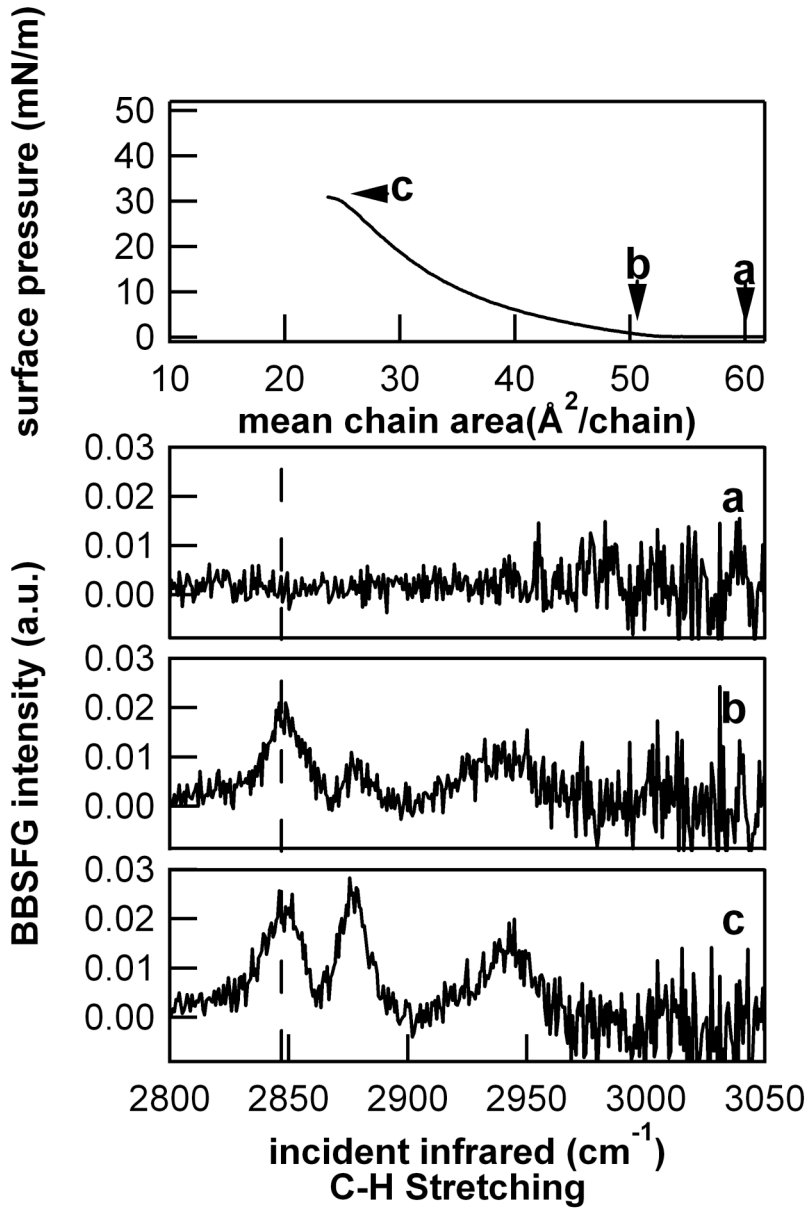

Figure 3.5. Concurrent Langmuir compression isotherm data and BBSFG spectra of an oleic acid monolayer at the air-water interface. The top graph is the Langmuir isotherm with markers indicating where BBSFG spectra are taken: (a) before beginning compression, (b) just after the first-order phase transition from the gas-liquid coexistence region evident at 51 Å^2/chain, and (c) just before film collapse at 28 Å^2/chain. Peaks in the BBSFG spectra are the CH_2 SS (2846 cm^{-1}), the CH_3 SS (2876 cm^{-1}), the CH_2 FR (2923 cm^{-1}), the CH_3 FR (2941 cm^{-1}), and the olefinic stretch at the carbon-carbon double bond (3014 cm^{-1}). The dashed line at 2846 cm^{-1} is a guide to the eye marking the CH_2 SS.

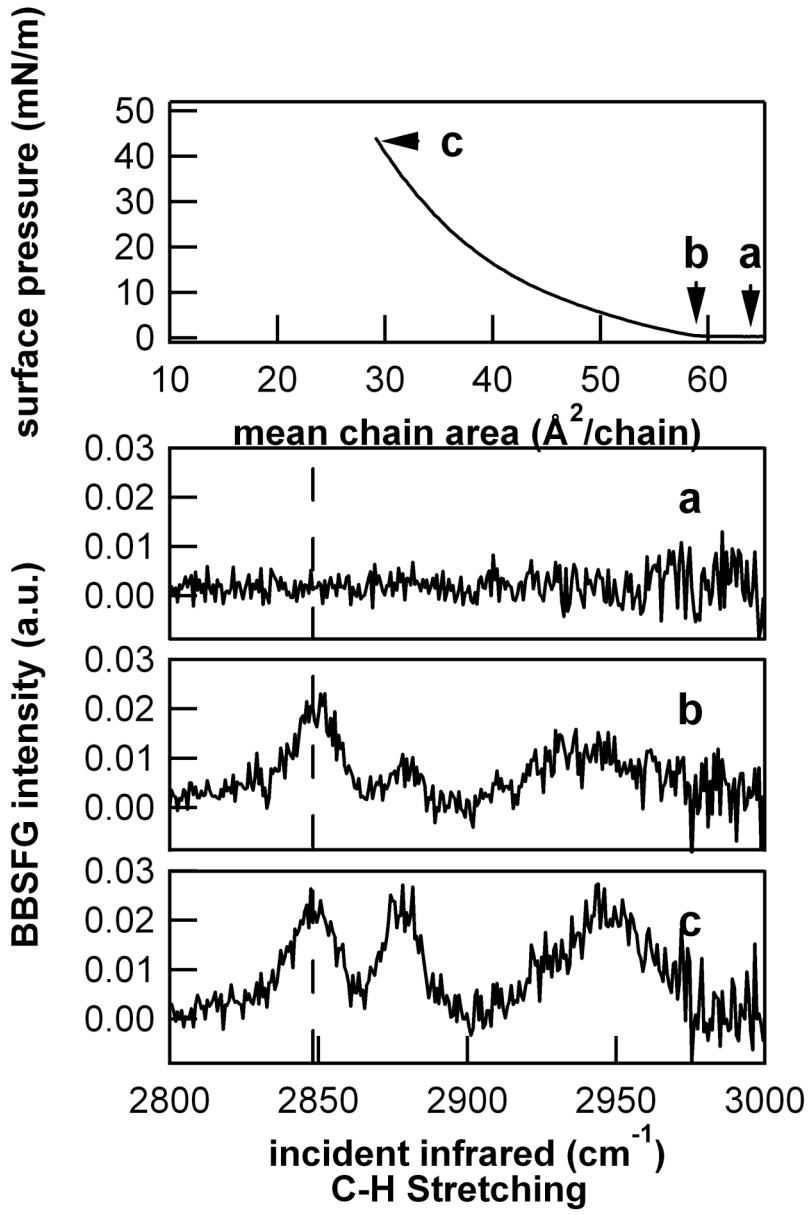

Figure 3.6. Concurrent Langmuir compression isotherm data and BBSFG spectra of a DOPC monolayer at the air-water interface. The top graph is the Langmuir isotherm with markers indicating where BBSFG spectra are taken: (a) before beginning compression, (b) just after the first-order phase transition from the gas-liquid coexistence region evident at 59 Å^2/chain, and (c) just before film collapse. The dashed line at 2846 cm^{-1} is a guide to the eye marking the CH_2 SS.

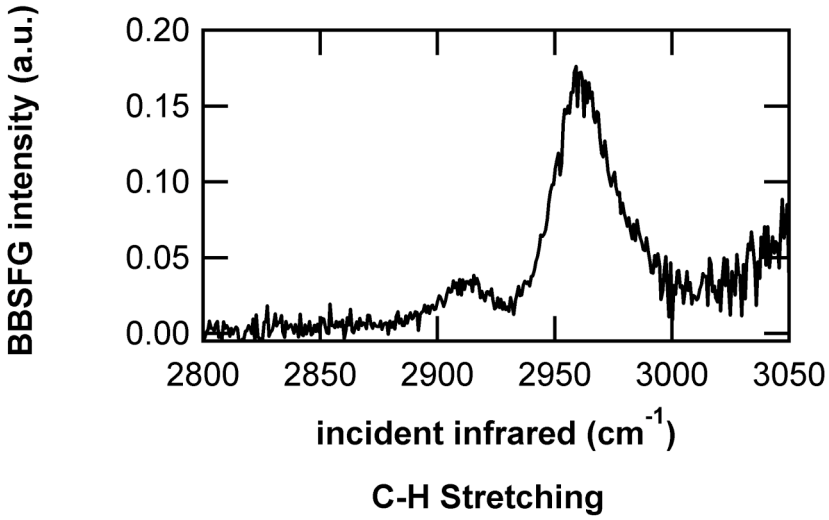

Figure 3.7. BBSFG spectra of protiated phosphocholine headgroup of d_{62}-DPPC. Peaks are the CH_2 SS at 2912 cm^{-1}, the CH_2 AS at 2950 cm^{-1}, and the choline (N-CH_3) SS occurring at 2974 cm^{-1} from the headgroup.

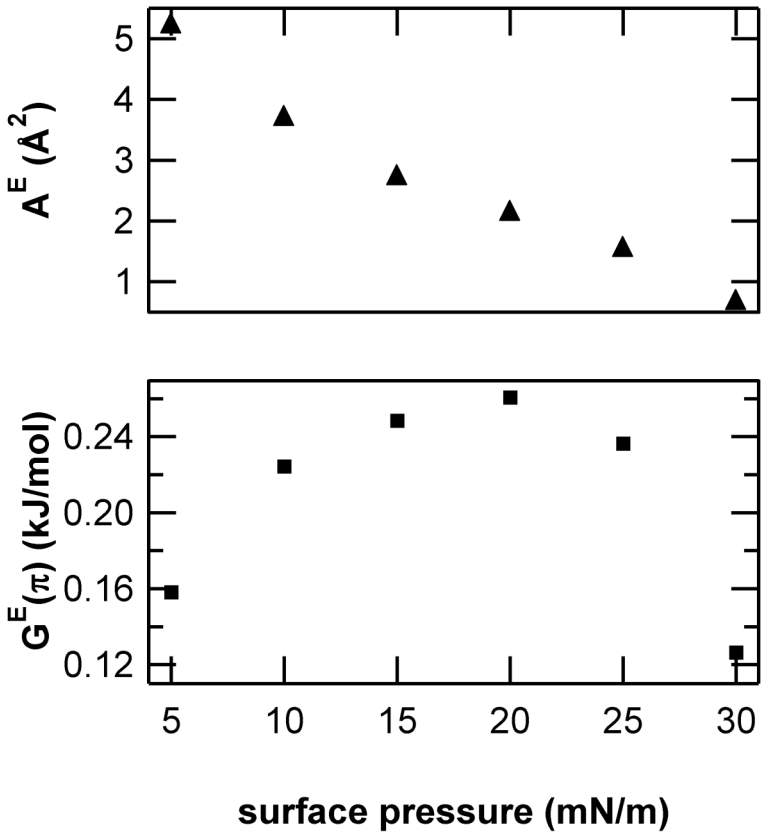

Figure 3.8. Excess area, A^E, and excess Gibbs energy of mixing, $G^E(\pi)$, for 1:1 oleic acid: d_{31}-palmitic acid monolayer.

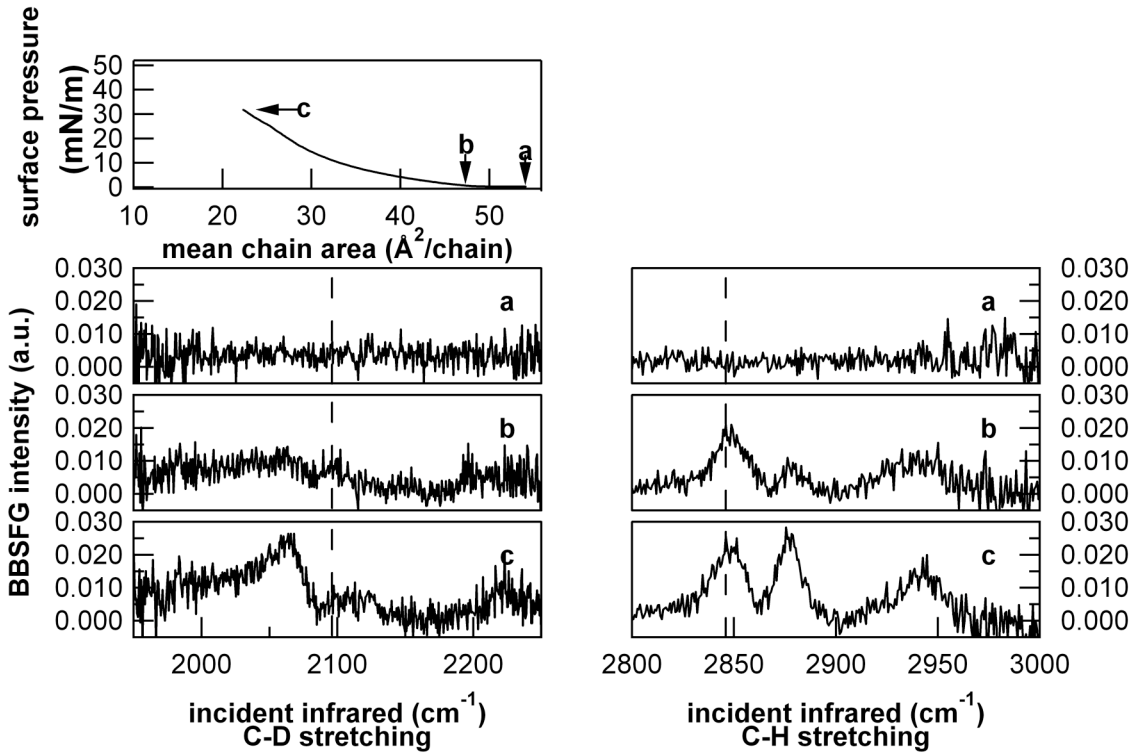

Figure 3.9. Concurrent Langmuir compression isotherm data and BBSFG spectra of the 1:1 oleic acid: d_{31}-palmitic acid monolayer at the air-water interface. The top graph is the Langmuir isotherm with markers indicating where BBSFG spectra are taken: (a) before beginning compression, (b) just after the lift-off where the surface pressure exceeds zero at 47 Å^2/chain, and (c) just before film collapse at 20 Å^2/chain. The dashed lines at 2096 and 2846 cm^{-1} are guides to the eye marking the CD_2 SS and the CH_2 SS, respectively.

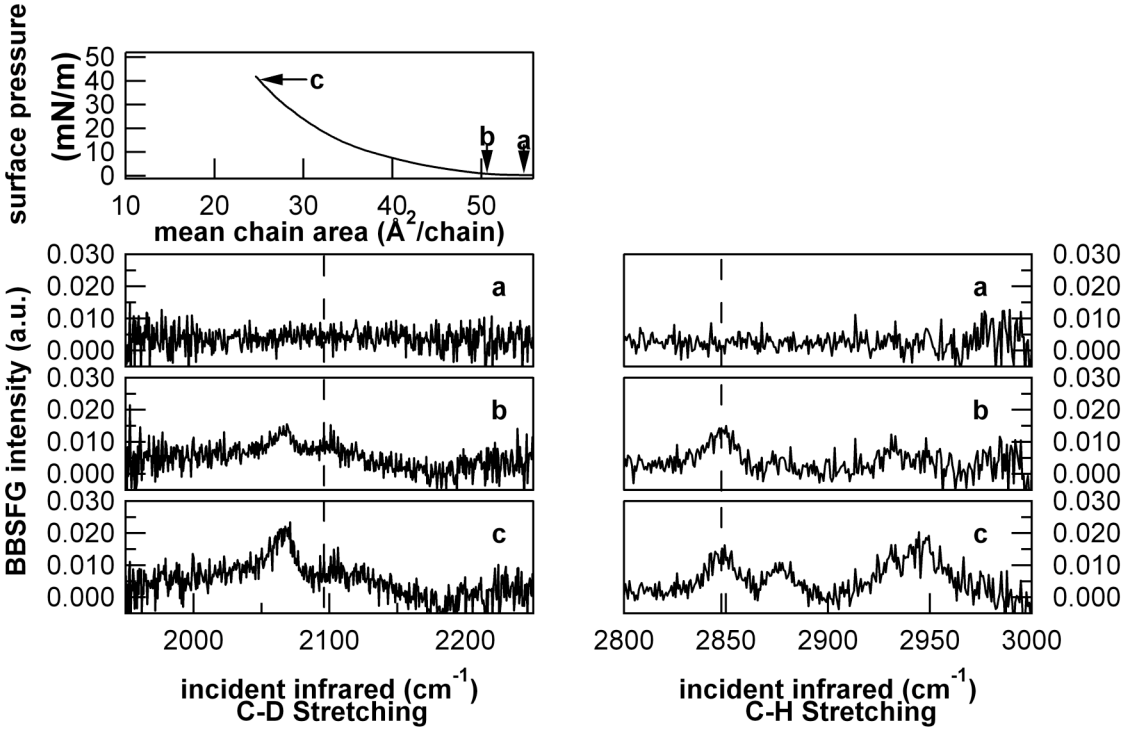

Figure 3.10. Concurrent Langmuir compression isotherm data and BBSFG spectra of the d_{31}-POPC monolayer at the air-water interface. The top graph is the Langmuir isotherm with markers indicating where BBSFG spectra are taken: (a) before beginning compression, (b) just after the first-order phase transition from the gas-liquid coexistence region to the liquid phase at 51 Å^2/chain, and (c) just before film collapse. The dashed lines at 2096 and 2846 cm^{-1} are guides to the eye marking the CD_2 SS and the CH_2 SS, respectively.

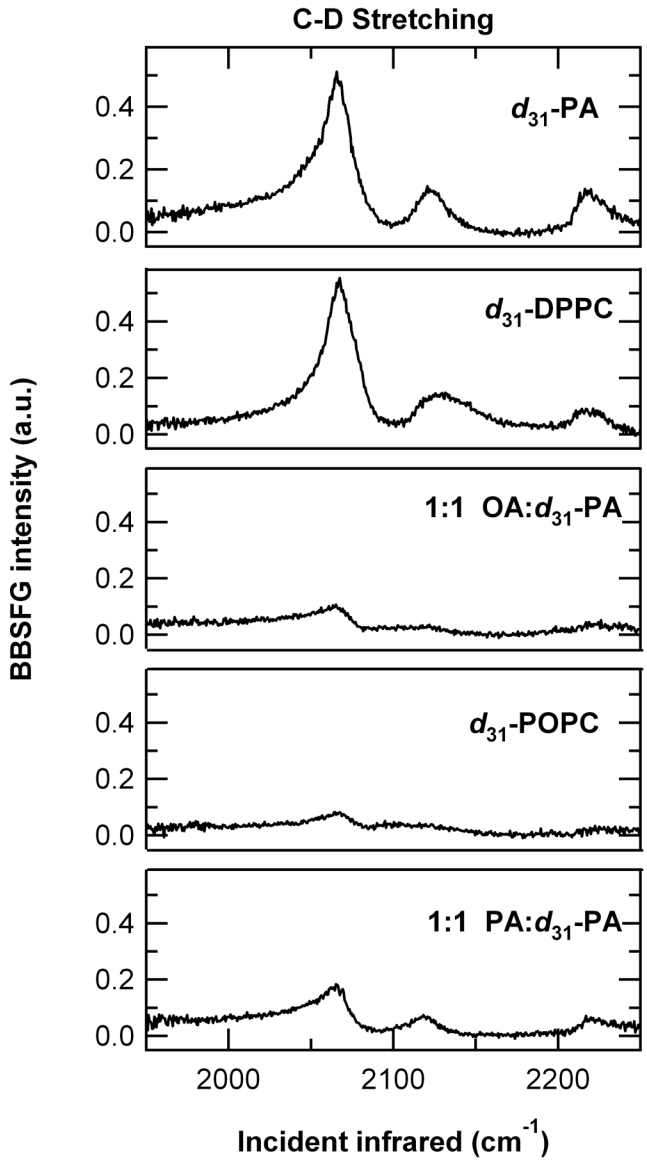

Figure 3.11. BBSFG spectra in C-D stretching region of pure and mixed monolayers taken with 2-minute spectral acquisition times.

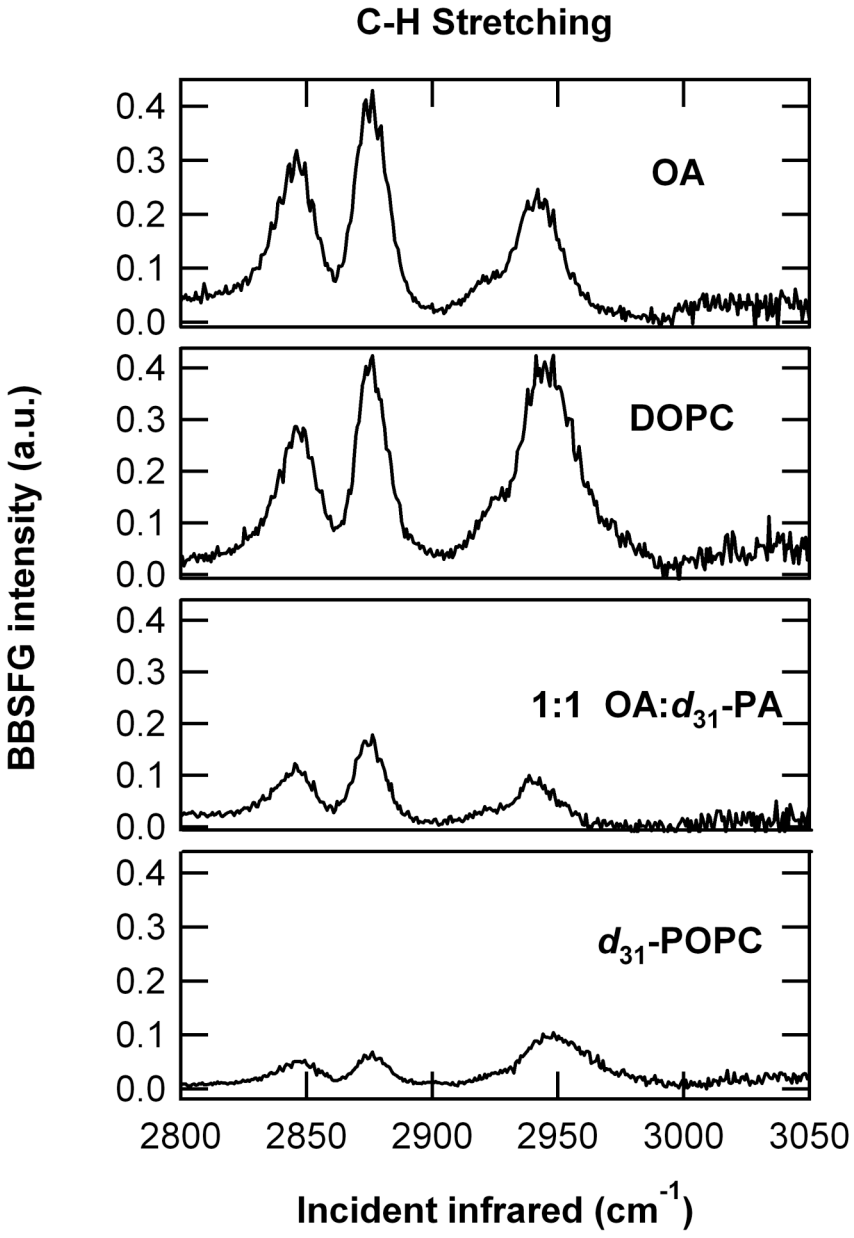

Figure 3.12. BBSFG spectra in C-H stretching region of pure and mixed monolayers taken with 2-minute spectral acquisition times.

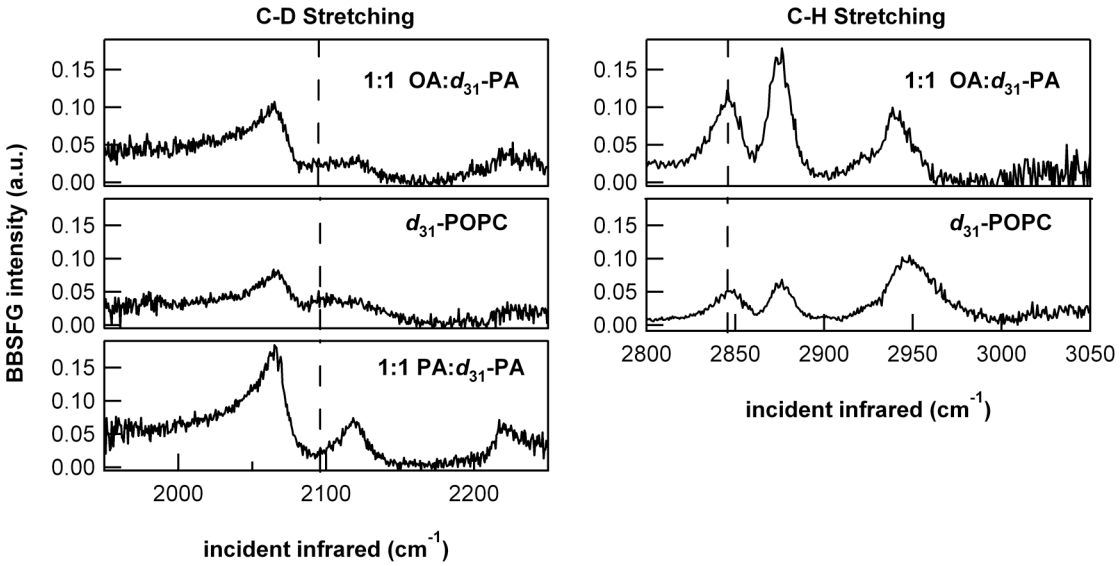

Figure 3.13. BBSFG spectra of mixed monolayers taken with 2-minute spectral acquisition times. The dashed lines at 2096 cm^{-1} and 2846 cm^{-1} are guides to the eye marking the CD_2 SS and the CH_2 SS, respectively.

CHAPTER 4

COMPETITION BETWEEN DPPC AND SDS AT THE AIR-AQUEOUS INTERFACE

In addition to the insoluble species present on the surface of fat-coated aerosols, surfactants of a more hydrophilic nature, such as oxidized organic compounds and shorter-chain hydrocarbons, likely exist both in the aqueous core and at the surface of atmospheric aerosols. The experiments presented here are a VSFG study of the interactions of a soluble organic surfactant and an insoluble lipid film at the air-aqueous interface. The soluble organic surfactant used is sodium dodecyl sulfate (SDS). The insoluble surfactant film found at the aerosol surface is modeled using a dipalmitoylphosphatidylcholine (DPPC) monolayer spread at the air-water interface.

4.1 Materials

1,2-dipalmitoyl-*sn*-glycero-3-phosphocholine (DPPC) and 1,2-dipalmitoyl-*sn*-glycero-3-phosphocholine-d62 (DPPC-d62) were obtained from Avanti Polar Lipids, Inc. (Alabaster, AL). Sodium dodecyl sulfate (SDS, 99+%, ACS reagent grade) and chloroform (≥ 99.8%, ACS spectrophotometric grade) were obtained from Sigma-Aldrich. Sodium dodecyl sulfate-d25 (SDS-d25, 98%) was obtained from Cambridge Isotope Laboratories, Inc. (Andover, MA). All chemicals were used as received.

Deionized water was obtained from a Barnstead Nanopure filtration system with a minimum resistivity of 18.2 MΩ-cm.

4.2 Experimental Method

Two types of experiments were performed to separately investigate the insoluble lipid film, DPPC or DPPC-d62, and the soluble surfactant, SDS or SDS-d25. Simplified structures of the deuterated species, DPPC-d62 and SDS-d25, are shown in Figure 4.1. To study the insoluble film, the lipid of interest (~1 mM DPPC or DPPC-d62 in chloroform) was spread on 20 mL of water in a petri dish using a 50-μL Hamilton syringe to form a monolayer at equilibrium spreading pressure. After waiting 10 minutes to ensure complete evaporation of chloroform and spreading of the lipid, VSFG spectra of the lipid monolayer at the air-water interface were obtained in relevant polarization combinations. SSP (S-polarized sum frequency, S-polarized visible, P-polarized infrared), SPS (S-polarized sum frequency, P-polarized visible, S-polarized infrared), and PPP (P-polarized sum frequency, P-polarized visible, P-polarized infrared) polarization combinations are used for these experiments.

Concentrated SDS or SDS-d25 solution (~17 mM in water) was injected into the water subphase using a 1-mL Hamilton syringe to form a 2 mM SDS subphase. To prevent disruption of the lipid monolayer during the injection process, the petri dish had a small glass tube (~0.3 cm diameter half-cylinder) attached vertically to its inner wall. The lower edge of the tube is approximately 0.5 cm above the bottom of the dish, and the upper edge of the tube is approximately 1 cm above the upper rim of the dish. The tube provides direct access to the subphase without requiring the needle to penetrate the lipid

monolayer at the air-water interface. After injection of SDS or SDS-d25, the VSFG signal of the lipid was monitored in SSP polarization combination until stability was observed. After stabilization of the signal, VSFG spectra were recorded in relevant polarization combinations, SSP, SPS, and PPP. The VSFG spectra of the lipid monolayer on the two subphases were compared.

Unlike the experiments used to probe the lipid molecules, in which the same sample was probed both before and after injection of SDS (or SDS-d25) into the subphase, the experiments used to probe the deuterated dodecyl sulfate chains compare two separate samples. In the first sample, concentrated SDS-d25 was injected into 20 mL of water in a petri dish to form a 2 mM SDS-d25 solution in the absence of the lipid monolayer. The second sample differs from the first sample only in that the lipid monolayer was present at the air-aqueous interface. For both samples, the VSFG signal (SSP polarization combination) from the deuterated dodecyl sulfate anions at the interface was monitored after injection until stability was achieved. Spectra were then obtained in relevant polarization combinations, SSP, SPS, and PPP, and compared for the two systems.

Approximately 4.5 uJ of infrared energy and 300 uJ of visible energy were used for these experiments. All reported spectra are the average of up to 3 2-minute acquisitions and are background-subtracted and normalized to the nonresonant VSFG signal from a GaAs crystal surface. The spectral bandwidth of the VSFG beam was >300 cm^{-1} in both the C-H and C-D stretching regions. Peak frequencies are reported as the observed frequencies, not from spectral fits.

4.3 Results and Discussion

To determine how the soluble surfactant SDS-d25 affects the molecules of a DPPC Langmuir monolayer at the air-aqueous interface, VSFG SSP spectra of a DPPC monolayer were obtained in the C-H stretching region both before and after injection of concentrated SDS-d25 into the water subphase and are shown in Figure 4.2a. Because the SDS-d25 molecules are fully deuterated, the VSFG signal originates solely from the DPPC molecules at the air-aqueous interface. VSFG spectra for all polarization combinations of the DPPC monolayer on water and SDS-d25 subphases are shown in Figure 4.2(a-c).

The observed peaks in Figure 4.2 have contributions from the vibrational resonances of both the acyl chains and the phosphocholine headgroups of the DPPC molecules. In the SSP spectrum of the DPPC monolayer on a water subphase (Figure 4.2a, black spectrum), the small peak at 2840 cm^{-1} is assigned to the CH_2 symmetric stretch (SS) of the acyl chains, the peak at 2872 cm^{-1} is assigned to the CH_3 SS of the acyl chains, the shoulder at 2905 cm^{-1} is assigned to the CH_2 Fermi resonance (FR) of the acyl chains with contribution from the CH_2 SS of the phosphocholine headgroups, and the peak at 2946 cm^{-1} has contributions from the CH_3 FR and CH_3 asymmetric stretch (AS) of the acyl chains and the CH_2 AS and CH_3 SS of the phosphocholine headgroups. In the spectrum of the DPPC monolayer on a 2 mM SDS-d25 subphase (Figure 4.2a, red spectrum), the peak at 2876 cm^{-1} is assigned to the CH_3 SS of the acyl chains, the shoulder at 2905 cm^{-1} is assigned to the CH_2 FR of the acyl chains with contribution from the CH_2 SS of the phosphocholine headgroups, and the peak at 2952 cm^{-1} has

contributions from the CH_3 FR and CH_3 AS of the acyl chains and the CH_2 AS and CH_3 SS of the phosphocholine headgroups.[32,34] The polarization data in Figure 4.2(b-c) are consistent with these assignments.[31]

Each acyl chain in a DPPC molecule has an even number (14) of CH_2 groups. For an all-*trans* configuration, adjacent methylene groups are in an anti conformation with all C-C bonds of the chain residing in the same plane. For such a configuration, local inversion symmetry exists between adjacent pairs of methylene groups in the acyl chains. The SS resonances of the CH_2 groups are not sum frequency active for an all-*trans* configuration since a lack of inversion symmetry is required for sum frequency activity.[28,35] The presence of a peak corresponding to the SS vibrations of the acyl chain CH_2 groups is a signature of conformational disorder in the chains. In Figure 4.2a, a peak assigned to the CH_2 SS of the acyl chains is present in the spectrum corresponding to the water subphase and is absent in the spectrum corresponding to the SDS-d25 subphase, indicating that the DPPC molecules are more conformationally ordered (i.e., have fewer gauche defects) in the presence of SDS-d25.

The increased VSFG intensity from 2975 cm^{-1} to 3050 cm^{-1} in the spectrum corresponding to the SDS-d25 subphase compared to that corresponding to the water subphase is assigned to aligned interfacial water molecules. The electrostatic field created at the interface by the charge on the sulfate headgroups of the deuterated dodecyl sulfate anions promotes increased alignment of the water molecules at the interface.[36]

Additional differences exist between the spectra in Figure 4.2a, but the multitude of vibrational resonances contributing to the observed peaks makes interpretation

difficult. Although analysis of additional polarization combinations, SPS and PPP, are helpful in deciphering vibrational assignments, these spectra do not allow complete deconvolution of the overlapping spectral resonances. Therefore, to separately determine the effect of SDS-d25 on the acyl chains and the phosphocholine headgroups of the lipid molecules, experiments using various combinations of DPPC-d62, SDS, and SDS-d25 in the C-H and C-D stretching regions were performed. The interfacial deuterated dodecyl sulfate anions were also investigated in the C-D stretching region in the presence and absence of a DPPC monolayer.

The vibrational resonances exclusively from the lipid headgroup are selectively probed in the C-H stretching region using a DPPC-d62 monolayer on both water and 2 mM SDS-d25 subphases, and the resulting spectra are shown in Figure 4.3. Because DPPC-d62 molecules have deuterated acyl chains and non-deuterated headgroups (refer to Figure 4.1), only the vibrational resonances of the DPPC-d62 headgroups are probed in these experiments. Figure 4.3a shows the VSFG spectra, SSP polarization combination, of the lipid monolayer both before (black spectrum) and after (red spectrum) injection of the concentrated SDS-d25 solution into the water subphase. VSFG spectra of the lipid headgroup on water and SDS-d25 subphases in all polarization combinations were obtained (Figure 4.3(b-c)), but are of insufficient signal/noise to provide insight beyond qualitative clarification of the spectral assignments.

Following the spectral assignments for the phosphocholine headgroup proposed by Conboy and co-workers,[32,34] peaks corresponding to the CH_2 SS (2909 cm^{-1}), the CH_2 AS (low frequency side of 2956 cm^{-1} peak), and the CH_3 SS (high frequency side of 2956

cm^{-1} peak) are present in the SSP spectra (Figure 4.3a) both before and after injection of the SDS-d25 into the subphase. In the spectrum of the DPPC-d62 headgroups on the SDS-d25 subphase (red spectrum), a broad VSFG intensity that increases with increasing wavenumber is assigned to the aligned interfacial water molecules caused by the charge of the deuterated dodecyl sulfate anions.[36] This broad intensity contributes to the enhancement of the observed DPPC-d62 headgroup peaks in the spectrum corresponding to the SDS-d25 subphase compared to those for the water subphase. The enhanced interfacial water signal in the presence of the soluble surfactant SDS-d25 is direct spectral evidence that SDS-d25 affects the air-aqueous interface even in the presence of a DPPC-d62 Langmuir monolayer.

The acyl chains of the lipid molecules are studied using a DPPC-d62 monolayer on both water and 2 mM SDS subphases in the C-D stretching region, and the resulting spectra are shown in Figure 4.4. Because the lipid headgroups are not deuterated in the DPPC-d62 molecules, only the vibrational resonances of the acyl chains are selectively probed in these experiments. In the SSP spectrum of the DPPC-d62 monolayer on water (Figure 4.4a, black spectrum), the peaks present correspond to the CD_3 SS (2070 cm^{-1}), CD_3 FR (2125 cm^{-1}), and CD_3 AS (2218 cm^{-1}) of the acyl chains of DPPC-d62.[19,27] The same vibrational resonances contribute to the peaks observed in the SSP spectrum of the monolayer on 2 mM SDS (Figure 4.4a, red spectrum).

The absence of VSFG intensity in the region corresponding to the CD_2 SS (approximately 2100 cm^{-1}) in both spectra shown in Figure 4.4a suggests that the lipid molecules are conformationally ordered in an all-*trans* configuration on both the water

and SDS subphases. However, this conclusion appears to be in direct conflict with the results of Figure 4.2a, where a peak assigned to the CH_2 SS of the acyl chains is readily observed for DPPC molecules on a water subphase. The presence of a CH_2 SS peak indicates that gauche defects are present in the acyl chains of the DPPC molecules on a water subphase. This inconsistency can be explained by a reduction in oscillator strength for deuterated methylene stretching modes compared to non-deuterated methylene stretching modes, which translates to improved detection limits for gauche defects in the acyl chains of the non-deuterated DPPC monolayer. Therefore, based on Figure 4.2a, DPPC molecules possess a detectable fraction of gauche defects in the monolayer on water.

In Figure 4.4a, the CD_3 SS peak in the spectrum corresponding to the lipid monolayer on the SDS subphase (red spectrum) has a lower intensity than in the spectrum corresponding to the water subphase (black spectrum). Because sum frequency intensity is a function of both number density and orientational order, the decrease in intensity of the CD_3 SS peak observed upon injection of SDS into the subphase must be a result of either a decrease in the number density of lipid molecules at the interface or a change in the orientation of the terminal methyl groups of the DPPC-d62 acyl chains.

As explained in detail by Ma and Allen,[28] the average angle of the C_{3v} axis of the terminal methyl groups of the DPPC-d62 acyl chains from the surface normal can be estimated using the ratio of equations 4.1 and 4.2 below.[37]

$$\chi^{(2)}_{SSP}(CD_3SS) = \tfrac{1}{2} N\beta_{ccc}[\cos\theta(1+r) - \cos^3\theta(1-r)] \tag{4.1}$$

$$\chi^{(2)}_{SSP}(CD_3AS) = -N\beta_{caa}[\cos\theta - \cos^3\theta] \tag{4.2}$$

$\chi^{(2)}_{SSP}(v)$ is the macroscopic second-order nonlinear susceptibility of the specified vibration ν in SSP polarization combination, N is the number density of interfacial molecules, β_{lmn} is the specified molecular hyperpolarizability, θ is the average orientation angle of the C_{3v} axis of the terminal methyl group from the surface normal, and r is the ratio $\frac{\beta_{aac}}{\beta_{ccc}}$. Here, r is equal to 2.3 [37] and $\frac{\beta_{caa}}{\beta_{aac}}$ is equal to 4.2. [38,39] The ratio of the susceptibilities of the CD_3 SS to the CD_3 AS is estimated experimentally by taking the square root of the ratio of the experimental VSFG intensities (component peak areas from spectral fits) of the CD_3 SS peak to the CD_3 AS peak. Using this method, θ is calculated to be 16.6 ± 0.6° for DPPC-d62 on water and 17.0 ± 0.6° for DPPC-d62 on 2 mM SDS. The small difference in θ calculated for the two subphases is well within the error of the calculation. Therefore, the average angle of the C_{3v} axis of the terminal methyl groups from the surface normal is virtually the same for the DPPC-d62 molecules on water and SDS subphases.

Because the angle between the C_{3v} axis of the terminal methyl group and the axis of the acyl chain is fixed for an all-*trans* chain configuration, a change in the tilt angle of the chains from the surface normal accompanies a change in θ. Assuming that the number of gauche defects in the lipid molecules is small for the water subphase and negligible for the SDS subphase, equivalent θ values for the DPPC-d62 molecules on the two subphases translates to equivalent chain tilt angles for the DPPC-d62 molecules on the two subphases. Because a significant change in the orientation of the DPPC-d62 molecules on the two subphases is not observed, the decrease in VSFG intensity for the

DPPC-d62 monolayer on the 2 mM SDS subphase compared to the water subphase is attributed to a decrease in the number density of DPPC-d62 molecules at the interface.

In addition to probing the lipid molecules in this mixed system, the soluble surfactant SDS-d25 was also probed in the C-D stretching region in both the presence and absence of a DPPC monolayer, and the resulting VSFG spectra are shown in Figure 4.5. Because sum frequency generation is an interface-selective spectroscopic technique, only the deuterated dodecyl sulfate chains at the air-aqueous interface contribute to the VSFG signal in these experiments. Additional changes to those described below have been observed to occur in the spectra over a longer period of time. Several additional processes that become important on longer time scales (adsorption of the surfactants to the glass dish, solubilization of the lipid, etc.)[40] make the interpretation complex and are beyond the scope of this discussion.

In the VSFG SSP spectrum of the SDS-d25 chains in the absence of a DPPC monolayer, shown in Figure 4.5a (black spectrum), the peak at 2070 cm^{-1} is assigned to the CD_3 SS with the shoulder at 2095 cm^{-1} assigned to the CD_2 SS, the peak at 2140 cm^{-1} is assigned to the CD_3 FR with some contribution from the CD_2 FR, and the peak at 2212 cm^{-1} is assigned to the CD_3 AS. The CD_2 FR and CD_2 AS of the interfacial SDS-d25 chains may contribute to the observed intensity in the 2150 – 2200 cm^{-1} region.[27] The presence of peaks assigned to SS resonances of the CD_2 groups indicates that the SDS-d25 chains possess some gauche defects and are not completely ordered at the interface. This result is in agreement with previous studies of SDS at the air-aqueous interface that report conformational disorder in the SDS chains even at maximum surface coverage.[41-43]

Although the VSFG signal from the SDS-d25 chains appears immediately after injection in the absence of a DPPC monolayer, the signal first appears approximately 30 minutes after injection in the presence of a DPPC monolayer. This indicates either a low number density of interfacial SDS-d25, a large degree of disorder in the interfacial SDS-d25, or a combination of these two phenomena occurs at the interface immediately after injection of SDS-d25 in the presence of a DPPC monolayer. Because each phosphocholine headgroup occupies approximately 50 $Å^2$ at the surface,[44] the initial space available for SDS-d25 at the liquid surface is limited. Over time, the SDS-d25 anions compete with the DPPC surface molecules and incorporate into the lipid monolayer, and VSFG signal is observed.

In Figure 4.5a, the red spectrum corresponds to interfacial SDS-d25 in the presence of a DPPC monolayer after temporary stability of the signal is achieved. This spectrum has similar features to the spectrum corresponding to the absence of DPPC (Figure 4.5a, black spectrum), but has a much lower intensity. The spectrum of the SDS-d25 chains corresponding to the absence of DPPC (black spectrum) shows significant asymmetry in the CD_3 SS peak due to the presence of a CD_2 SS shoulder. However, the spectrum corresponding to the presence of DPPC (red spectrum) has a more symmetric CD_3 SS peak, indicating a lower proportion of gauche defects and a slight increase in conformational order of the interfacial SDS-d25 chains in the presence of the lipid monolayer. This result is consistent with the observation by Meister and co-workers of a small increase in the order of SDS molecules incorporated into a DMPC-d54 monolayer using reflection-absorption infrared spectroscopy.[41] A possible explanation for the

increase in conformational order of the SDS-d25 chains is that the presence of the lipid monolayer at the liquid surface sterically hinders the interfacial SDS-d25 chains from adopting disordered conformations with many gauche defects. Because an increase in order is expected to increase the VSFG signal, the lower signal observed for SDS-d25 in the presence of a DPPC monolayer compared to that observed in the absence of a DPPC monolayer is attributed to a lower number density of interfacial SDS-d25. However, reduction in the overall DPPC-d62 monolayer spectral intensity observed for the SDS subphase compared to the water subphase in Figure 4.4a indicates that the soluble surfactant does, in fact, replace a fraction of the lipid molecules in the monolayer.

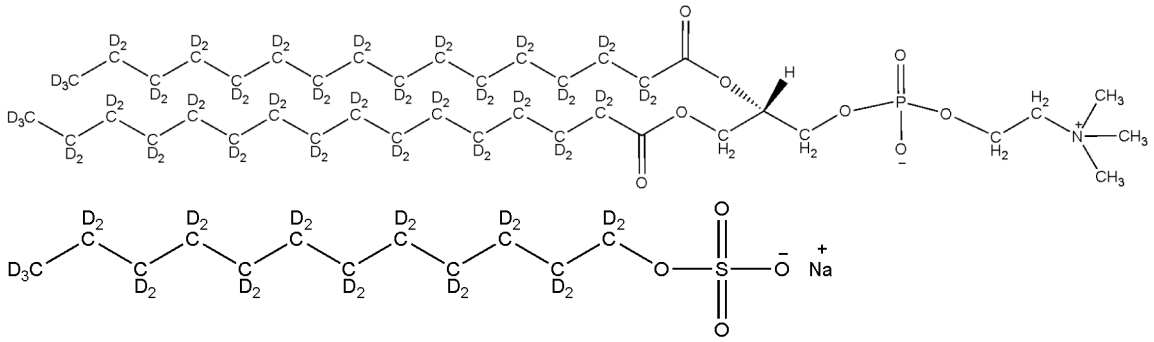

Figure 4.1. Simplified structures of DPPC-d62 (top) and SDS-d25 (bottom).

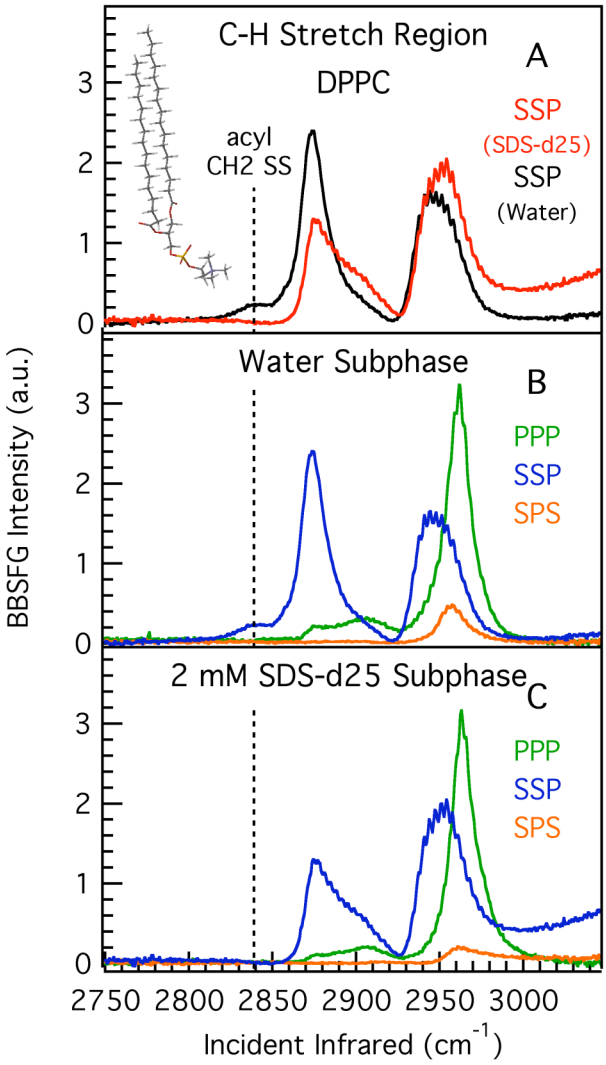

Figure 4.2. VSFG spectra of DPPC molecules in C-H stretching region: (A) SSP polarization combination: water subphase (black) and 2 mM SDS-d25 subphase (red); (B) water subphase: SSP (blue), PPP (green), and SPS (orange); and (C) 2 mM SDS-d25 subphase: SSP (blue), PPP (green), and SPS (orange).

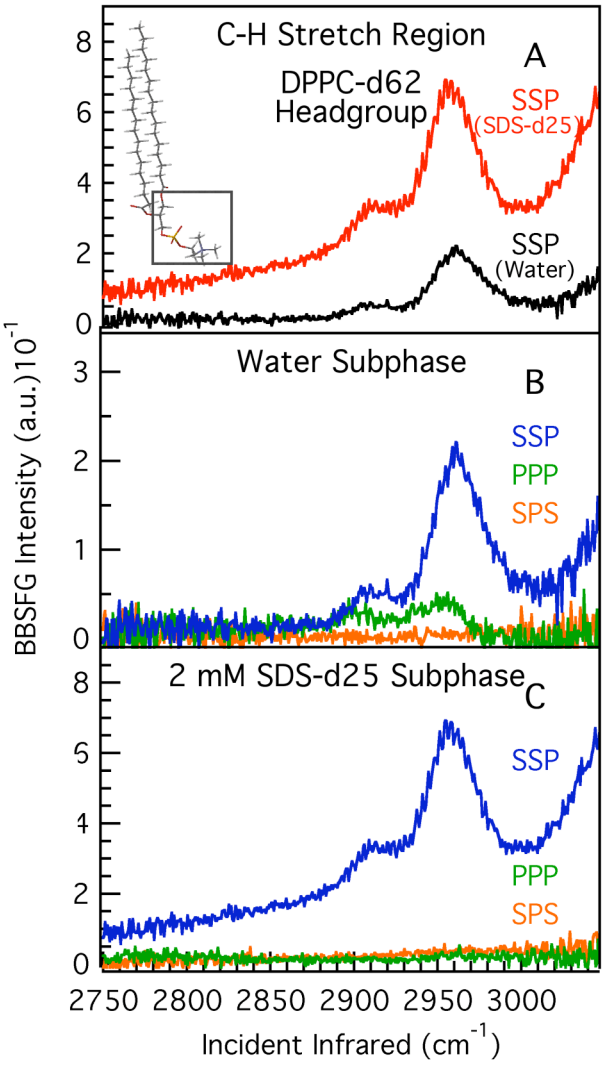

Figure 4.3. VSFG spectra of headgroups of DPPC-d62 in C-H stretching region: (A) SSP polarization combination: water subphase (black) and 2 mM SDS-d25 subphase (red); (B) water subphase: SSP (blue), PPP (green), and SPS (orange); and (C) 2 mM SDS-d25 subphase: SSP (blue), PPP (green), and SPS (orange).

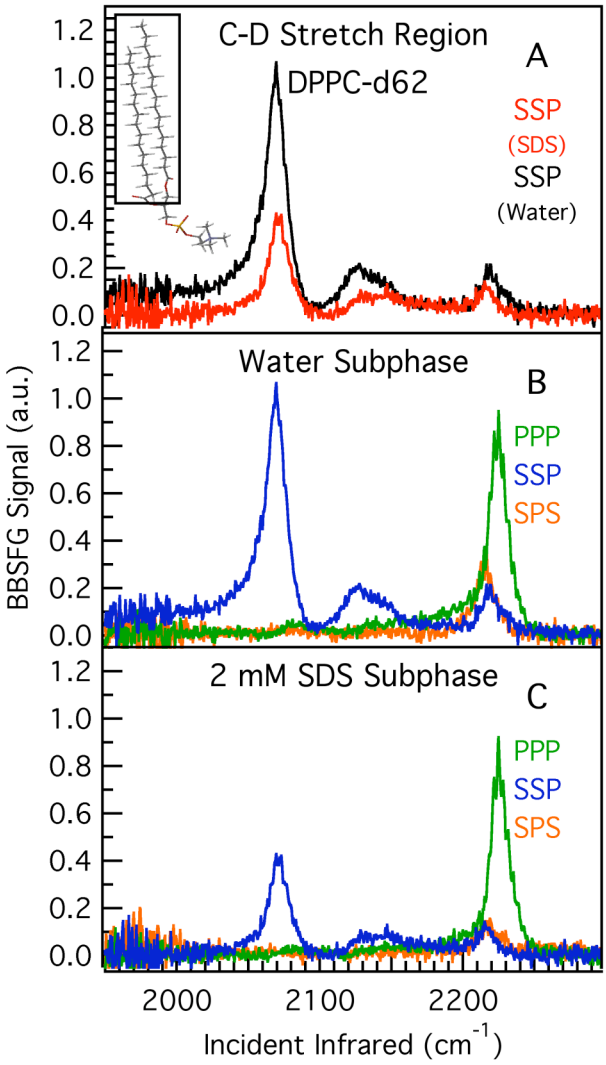

Figure 4.4. VSFG spectra of acyl chains of DPPC-d62 in C-D stretching region: (A) SSP polarization combination: water subphase (black) and 2 mM SDS-d25 subphase (red); (B) water subphase: SSP (blue), PPP (green), and SPS (orange); and (C) 2 mM SDS-d25 subphase: SSP (blue), PPP (green), and SPS (orange).

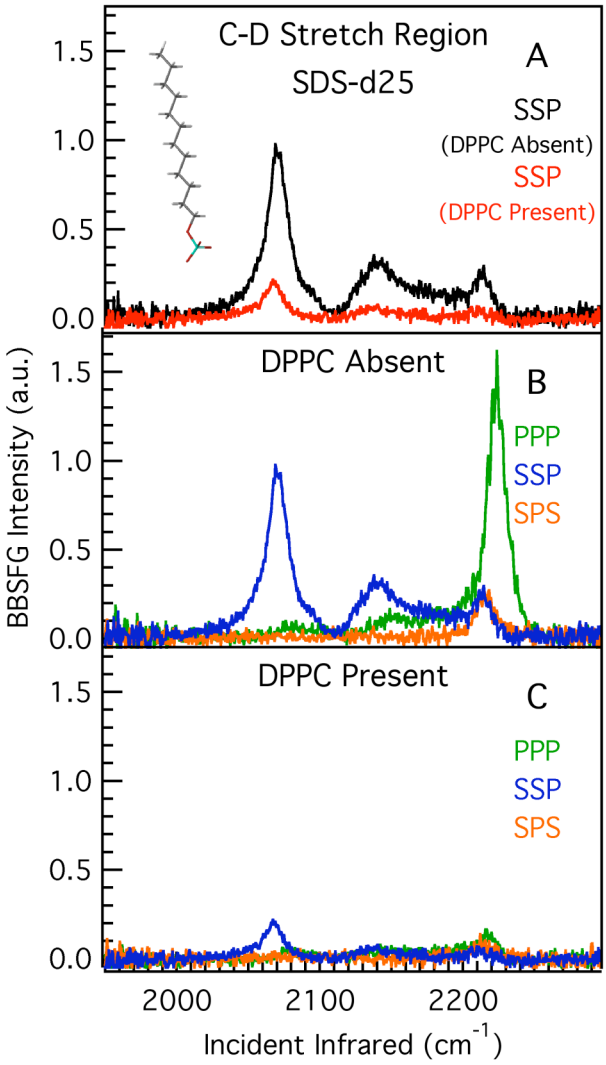

Figure 4.5. VSFG spectra of SDS-d25 chains in C-D stretching region: (A) SSP polarization combination: in absence (black) and presence (red) of DPPC monolayer; (B) in absence of DPPC monolayer: SSP (blue), PPP (green), and SPS (orange); and (C) in presence of DPPC monolayer: SSP (blue), PPP (green), and SPS (orange).

CHAPTER 5

SURFACE RESIDENCE AND UPTAKE OF ALKYL HALIDES AND ALCOHOLS AT THE AQUEOUS SURFACE

Halogenated organic compounds of both biogenic and anthropogenic origin are abundant in the atmosphere and have been recognized to play important roles in both tropospheric and stratospheric chemistry.[1] Of the alkyl halides, methyl chloride (MeCl) is of particular interest because it is the largest contributor of organic chlorine to the atmosphere[45,46] with an average tropospheric mixing ratio of approximately 540 pptv.[47,48] A significant fraction of the MeCl present in the atmosphere is biogenic in origin,[47,48] and a great deal of research in recent years has been focused on balancing the global MeCl budget because the known sinks of MeCl outweigh the known sources.[46,47,49] The primary sources of MeCl that are currently known include biomass burning,[50] wood-rot fungi,[51] tropical coastal land,[52] various tropical plants,[53] coastal salt marshes,[54,55] and the ocean,[47,56] which also serves as a net sink of MeCl at high latitudes.[56,57] In the troposphere, the primary sink of MeCl is reaction with OH radical.[47] However, the relatively long tropospheric lifetime of MeCl (>1 year) results in a significant amount of

MeCl being transported into the stratosphere, where it undergoes photolysis to release ozone-destroying Cl atoms.[46,58]

Likewise, halides have also been implicated in the destruction of ozone in the troposphere. For several years, surface-level ozone depletion events have been observed in the Arctic at polar sunrise and have been correlated to an increase in gas-phase Br atom concentration, suggesting that atomic Br is an important component in the ozone destruction cycle.[59-63] However, the mechanisms for production of Br atom and its precursors have not been fully elucidated, nor have the chemical identities of the precursors been determined with great certainty.[64] One of the first mechanisms proposed for initiation of the ozone depletion event was photolysis of gas-phase bromoform.[59] Although it has subsequently been suggested that this pathway is not significant enough to account for the degree of ozone destruction,[65] the possible role of halogenated organic species, such as alkyl halides, in such processes must not be overlooked.

Alternatively, oxidation of halide ions in sea salt aerosol, the frozen ocean surface, and the Arctic snow pack has been postulated as a possible pathway to the formation of reactive Br species involved in the ozone depletion events.[66,67] Both bulk aqueous-phase and heterogeneous reactions have been shown to be important in the postulated mechanisms.[64-70] Because the concentration of halide ions is enhanced at the surface of sea salt aerosols and in frost flowers on the frozen ocean surface compared to bulk-phase seawater,[2,71-73] interfacial processes leading to the activation of halides and other surface species must be considered for other atmospheric processes as well.

Considering that the known geochemical cycle of MeCl involves partitioning between different phases, it is reasonable that alkyl halides might also participate in interfacial processes. Alkyl halide species have been observed in the Arctic, where the potential for interfacial chemistry on aerosols, the open ocean, the snow pack, and the quasi-liquid layer of ice is significant.[74]

Here, VSFG is used to study the residence and surface organization of gas-phase MeCl onto the surface of water. In addition, Raman spectroscopy is used to study the uptake of MeCl into the bulk aqueous phase. These experiments are performed as necessary first steps in understanding possible surface reactivity and multi-phase partitioning of alkyl halides. The results obtained for MeCl are compared to those obtained for methyl alcohol (MeOH), which is also present in the Arctic troposphere.[75] Recent field observations indicate that MeOH is taken up into the interstitial air of the porous snow pack, where the surface area of the snow pack in contact with air is substantial.[75] Preliminary data of a study of a longer-chain series, comprising n-butyl chloride (BuCl), n-butyl bromide (BuBr), and n-butyl alcohol (BuOH) is also presented.

5.1 Materials

Methyl alcohol (CH_3OH; HPLC grade), n-butyl chloride ($CH_3(CH_2)_3Cl$; ACS certified), and n-butyl alcohol ($CH_3(CH_2)_3OH$; ACS certified) were obtained from Fisher Scientific. n-Butyl bromide ($CH_3(CH_2)_3Br$; 99+% purity) was obtained from Acros Organics. Methyl chloride (CH_3Cl; 99.5% purity, instrument grade) was obtained from Scott Specialty Gases, Inc. (Plumsteadville, PA). Nitrogen (NF, compressed) was obtained from Praxair, Inc. (Danbuy, CT). All chemicals were used as received.

Deionized water was obtained from a Barnstead Nanopure filtration system with a minimum resistivity of 18.2 MΩ-cm.

5.2 Experimental Method

To monitor the adsorption of gas-phase alcohols and alkyl halides to the aqueous surface, a flow chamber was used in combination with the BBSFG system described in Chapter 2. The flow chamber was attached to the sample stage of the BBSFG system, and the gas-phase species of interest was flowed over 24 mL of water in a petri dish contained in the chamber while continuous VSFG spectra (60-second acquisitions) were obtained for up to two hours. Approximately 4.5 μJ of infrared energy and 300 μJ of visible energy were used for these experiments, and all spectra were obtained in SSP polarization combination. Background spectra were obtained periodically throughout the flow experiments by disrupting the temporal overlap of the incident beams. All VSFG spectra are background-subtracted and normalized to the nonresonant VSFG signal from a GaAs crystal.

The chamber used for the adsorption experiments is comprised of a stainless steel lid that attaches to a stainless steel cylindrical base by using knife-edge sealing technology in conjunction with a copper gasket (4-inch I.D.). The incident beams enter the chamber through a BaF_2 viewport (Reflex Analytical Corp., p/n 8960-1BAF2) on the chamber lid, and the SFG beam exits the chamber through a BK7 viewport (Kurt J. Lesker Co., p/n VPZL-275BK7). Because the optical properties of the windows affect the spatial and temporal overlap of the incident beams inside the flow chamber (compared to when the chamber lid is removed), the overlap of the beams was optimized

while monitoring the VSFG signal from a sample of SDS inside the flow chamber before the adsorption experiments were performed. The base of the chamber was lined with Teflon tape to minimize scattering of light inside the chamber, and a Teflon ring was used around the petri dish to hold the sample in place inside the chamber.

Volatilization of the liquid samples (MeOH, BuOH, BuCl, and BuBr) was accomplished by flowing nitrogen gas at 15 sccm through the liquid of interest contained in a glass vial. A flow controller (MKS Instruments, model 1479A51CS1BM; used with control box model PR4000-F2V1N) was used to maintain a steady flow of nitrogen gas into the liquid sample. Teflon tubing (1/8-inch O.D.) and Swagelok fittings were used to connect the flow controller to a stainless steel needle that was inserted into the liquid sample through a rubber septum. The nitrogen gas was bubbled into the liquid sample, and the gas mixture (volatilized species and nitrogen gas) was transported out of the vial and into the flow chamber using a second needle attached to Teflon tubing (1/4-inch O.D.). The opening of the second needle was placed approximately 1 inch above the surface of the liquid sample. Swagelok fittings were used to attach the tubing to both the collection needle and to an inlet port in the flow chamber lid.

Because MeCl has a very high vapor pressure at room temperature, the liquid was contained in a non-pressurized tank. The MeCl vapor was extracted from the container using a low-pressure regulator (Scott Specialty Gases, Inc., model 051202A510). Teflon tubing (1/4-inch O.D.) connected the regulator to a flow controller that was operated at 10 sccm. The output of the flow controller was connected to the flow chamber using Teflon tubing (1/4-inch O.D.).

For all species, the experiments were performed at 24°C and ambient pressure, and the vapor was exhausted from the flow chamber through an outlet on the lid. The organic vapors were purged from the cell using a flow of pure nitrogen gas after the adsorption experiments. The aqueous samples were then collected and stored for subsequent bulk-phase analysis using a Raman spectrometer.

The Raman spectrometer employed in these experiments uses a 785 nm continuous wave laser (Process Instruments; model PI-ECL-785-300-SH) as an excitation source. The laser beam (200 mW) is delivered to the sample by the same fiber optic probe (InPhotonics) used to collect the scattered light. The scattered light is dispersed by a 600 g/mm grating blazed at 1 μm in a 500 mm monochromator (Acton Research, SpectraPro 500i; 50 μm slit width) and detected using a liquid nitrogen-cooled CCD (Roper Scientific, LN 400EB, back-illuminated, deep depletion, 1340 x 400 pixel array). The monochromator is controlled using SpectraSense software (Acton Research, version 4.2.9) and calibrated to the 435.83 nm line of fluorescent light. The peak positions of the Raman spectra are calibrated by comparing the position of experimentally observed naphthalene peaks to those in the literature. An acquisition time of 2 minutes was used for the Raman experiments. All reported peak frequencies (for both Raman and VSFG spectra) are the observed frequencies, not from spectral fits.

5.1 Results and Discussion

The VSFG spectra obtained from the flow experiments of MeOH (left panel) and MeCl (right panel) over an aqueous surface are shown in Figure 5.1. In the spectrum of adsorbed MeOH, the peak at 2835 cm^{-1} is assigned to the CH_3 SS and the peak at 2948

cm^{-1} is assigned to a CH_3 FR with the shoulder at 2912 cm^{-1} assigned to a second CH_3 FR. These assignments are consistent with those for the VSFG spectra of neat MeOH and aqueous MeOH solutions reported by Ma and Allen.[76] Because sum frequency intensity is a function of both number density and orientational order, the presence of peaks in the VSFG spectrum of MeOH at the water surface suggests that the adsorbed MeOH molecules are not completely disordered at the air-aqueous interface, but rather have a preferential orientation at the interface. Molecular dynamics studies of short-chain alcohols at the air-aqueous interface indicate that the hydroxyl group of the alcohol hydrogen-bonds to the surface water molecules.[77-80] This suggests that the preferential orientation of short-chain alcohols at the air-aqueous interface is such that the hydrophilic hydroxyl group associates with the aqueous phase and the hydrophobic alkyl group points into the gas phase. Thus, the MeOH molecules adsorbed at the air-aqueous interface adopt an organized surface structure.

In comparison, no peaks are observed in the VSFG spectrum of MeCl at the air-aqueous interface, indicating that MeCl either does not adsorb to the aqueous surface upon collision or does adsorb to the aqueous surface, but has a low number density, disordered interfacial arrangement, very short surface residence time, or some combination of these phenomena. Understanding the possible uptake of MeCl molecules from the gas phase into the bulk aqueous phase can aid in understanding the adsorption of MeCl to the aqueous surface.

To determine whether MeCl is taken up into the bulk liquid phase from the gas phase, the Raman spectrum of the bulk sample was obtained after the flow experiment

and is shown in Figure 5.2 (red spectrum). A peak at 710 cm^{-1} is observed in the Raman spectrum of the aqueous MeCl sample and is assigned to the C-Cl stretch of MeCl.[81] The presence of a peak attributed to MeCl in the spectrum of the bulk aqueous phase is direct evidence that MeCl is taken up into the aqueous phase from the gas phase during the flow experiments. The Raman spectrum of a bulk aqueous sample after a MeOH flow experiment is shown in this frequency range for comparison (Figure 5.2, blue spectrum). No peaks from MeOH are expected or observed in this frequency range, and comparison of the two spectra in Figure 5.2 shows that the C-Cl stretch peak from MeCl is significant. Uptake of gas-phase MeOH into the bulk aqueous phase has been reported previously.[82]

Although MeCl is not detected at the interface during the VSFG experiments (within the detection limits of the BBSFG system under the experimental conditions used), the Raman bulk-phase studies indicate that some interaction of the gas-phase molecules with the aqueous interface must occur because uptake of MeCl from the gas phase into the aqueous phase is observed (as is evident in Figure 5.2). To explain these results, a convolution of orientation and number density must be considered.

By a simple comparison of electronegativities, the C-Cl bond in MeCl is expected to be more polar than the C-H bonds. Based on this model, the more hydrophilic C-Cl bond would preferentially associate with the aqueous phase compared to the more hydrophobic C-H bonds, which would be expected to be oriented more toward the vapor phase. This orientation has been observed for MeCl adsorbed to a layer of D_2O pre-adsorbed to Pd(111).[83] In this VSFG study, the authors determined that the Cl atom of

MeCl hydrogen-bonded to the D atoms of the pre-adsorbed D_2O molecules, resulting in a net orientation of MeCl molecules at the surface. Because water molecules adsorbed to Pd(111) are well-ordered over several monolayers, forming a noncentrosymmetric water layer,[83] the surface structure of MeCl may be different on the surface of a bulk aqueous sample than on the surface of water adsorbed to a metal, so caution must be exercised in extrapolating these results to the study presented here. Nonetheless, intuition dictates that the geometry adopted by MeOH at the aqueous surface, in which the more hydrophilic moiety associates with the aqueous phase, is also likely to be adopted by MeCl molecules adsorbed at the aqueous surface. Thus, it is likely that a low number density of MeCl molecules at the surface plays some role in the absence of VSFG signal for this system.

Several possibilities can lead to a low number density of interfacial MeCl molecules, including a low probability of adsorption upon collision, fast desorption from the surface for those molecules that do adsorb upon collision, or fast solvation of adsorbed molecules (i.e., fast uptake of adsorbed molecules into the bulk phase). The last two of these possibilities would lead to a short residence time of adsorbed MeCl molecules. Because MeCl is soluble in water,[84] it is not unreasonable to suggest that solvation of MeCl is fast, contributing to a low number density of interfacial molecules. Because MeOH, which is fully miscible with water, is observed at the interface using VSFG, it is apparent that a convolution of both order and number density must be invoked to describe the adsorption and uptake processes for these two species. Although several questions remain to be answered regarding the adsorption and uptake of MeCl

and MeOH, the studies presented indicate that different mechanisms are responsible for determining the surface structures of MeOH and MeCl.

Comparison of the VSFG and Raman data for MeCl and MeOH (presented in Figures 5.1 and 5.2) with complementary studies of water-insoluble species might help to elucidate the mechanisms of adsorption and uptake for the halide and alcohol species. The complementary VSFG studies were performed on the complementary butyl species, and the results are presented below as preliminary data. Both BuCl and BuBr are insoluble in water, while BuOH has a solubility of 115 g/L. [84]

VSFG spectra of the flow experiments using the longer-chain series (BuOH-left panel, BuCl-center panel, and BuBr-right panel) are shown in Figure 5.3. The same trend is observed for the butyl species as is observed for the methyl species. No VSFG intensity is observed for the halides, but peaks are observed in the VSFG spectrum for the alcohol. The peaks in the VSFG spectrum obtained for the flow experiment of BuOH over water are assigned to the CH_2 SS (2845 cm^{-1}), CH_3 SS (2875 cm^{-1}), CH_2 FR (2911 cm^{-1}), and CH_3 FR (2945cm^{-1}). These assignments are based on VSFG assignments for neat BuOH in the literature.[31] As with MeOH, the VSFG spectrum of BuOH at the water surface suggests that the adsorbed BuOH molecules are not completely orientationally disordered at the interface. The presence of a peak corresponding to the CH_2 SS indicates that the adsorbed BuOH molecules possess some gauche defects. This finding is consistent with results reported in the literature.[31] Again, a convolution of orientation and number density prevents VSFG signal from being observed in the case of the butyl halide species.

As with the methyl species, Raman studies are necessary to probe the uptake of the butyl species into the bulk aqueous phase. These experiments are left for future study. To accurately compare the differences in uptake from the gas phase to the aqueous phase between the various species, the flow experiments must be standardized to deliver the same rate of molecules impinging on the surface for each species studied. The results of these studies will allow comparisons to be drawn based on the functionality (alcohol versus halide), identity of the halide (bromide versus chloride), and length of the alkyl chain (methyl versus butyl).

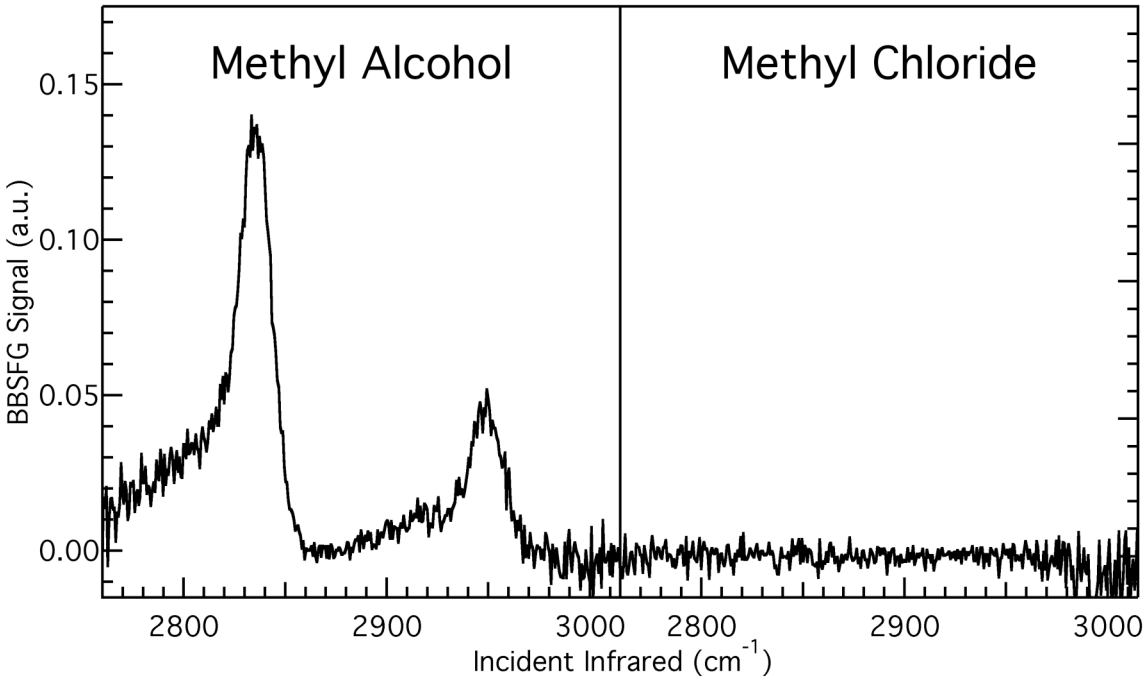

Figure 5.1. VSFG spectra from flow experiments over water: methyl alcohol (left panel) and methyl chloride (right panel) adsorbed to the aqueous surface.

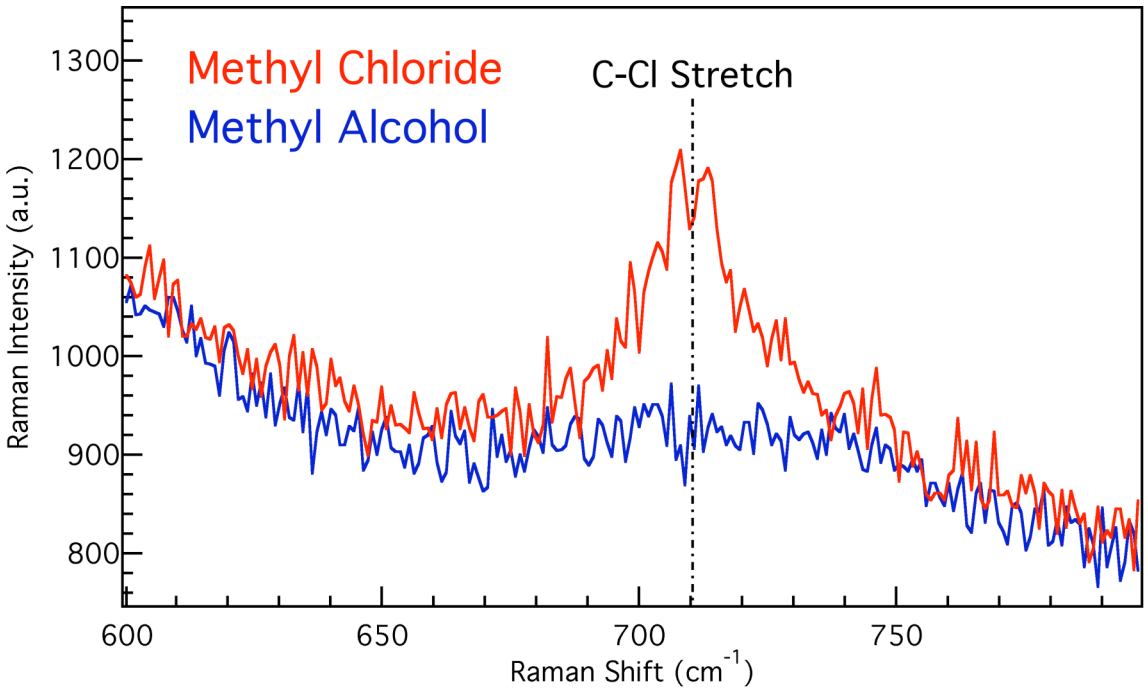

Figure 5.2. Raman spectra of bulk aqueous phase after flow experiments: methyl chloride (red) and methyl alcohol (blue).

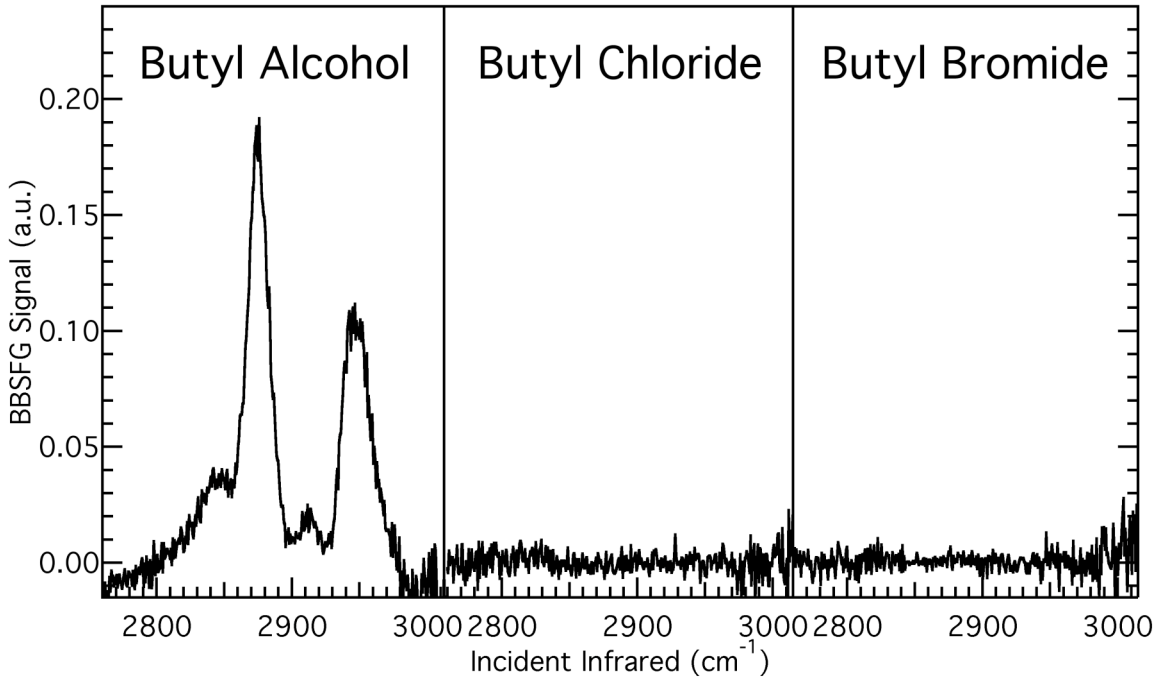

Figure 5.3. VSFG spectra from flow experiments over water: butyl alcohol (left panel), butyl chloride (center panel), and butyl bromide (right panel) adsorbed to the aqueous surface.

CHAPTER 6

CONCLUSION

The experiments presented in this thesis demonstrate the importance of interfacial interactions in atmospherically relevant model systems. Interactions between molecules in an insoluble film at the air-water interface and the influence of film composition on the structure of the surface were studied. Phase segregation is observed in a 1:1 mixture of oleic and palmitic acids, and the oleic acid molecules are observed to influence the structure of the palmitic acid molecules that are in close association. Similarly, interactions between an insoluble film at the air-water interface and a soluble surfactant in the aqueous bulk phase were probed. The soluble surfactant, SDS, replaced a fraction of the DPPC molecules at the interface and increased the conformational ordering of the DPPC acyl chains. The results of these studies indicate that the molecular composition of both the aerosol surface and aqueous core can affect the surface structure of the aerosol, which has the potential to affect the processing of the aerosol in the atmosphere. The adsorption and uptake of atmospherically important gas-phase species by an aqueous surface were also explored. Although uptake of gas-phase methyl chloride is observed in bulk phase analysis by Raman spectroscopy, a convolution of residence time, number

density, and orientational disorder prevent detection of methyl chloride adsorbed to the aqueous surface by VSFG. These results indicate that methyl chloride has the potential to participate in interfacial processes in the atmosphere. Details of these studies are available in Chapters 3-5, and an overview of the results is presented here.

The structure and interactions of the molecules that constitute lipid films, such as those that occur in biogenic atmospheric aerosols, were probed. By coupling a Langmuir trough with VSFG spectroscopy, the formation of monolayers at the air-water interface was investigated. Both the thermodynamic and spectroscopic data reveal that domain formation occurs in the 1:1 mixture of oleic acid and palmitic acid. Spectroscopic evidence indicates that the edges of the palmitic acid domains are perturbed by the oleic acid. Evidence of surface aggregation of palmitic acid and oleic acid monolayers spread from a 1:1 solution indicates that these species would also phase separate in naturally occurring surfactant systems, such as the monolayers found on fat-coated aerosols. Although the species phase segregate, the oleic acid can still disrupt the packing of the palmitic acid around the edges of the aggregates. The influence that *cis* oleic acid has on the conformations of palmitic acid molecules demonstrates that the composition of the film influences the structure of the film, which might have important consequences in how the aerosol is processed in the atmosphere. Comparing the monolayers formed from fatty acids with their corresponding phosphocholines indicates where the change in orientation of the hydrophilic headgroup occurs during the compression isotherm of the monolayer.

An investigation of the interactions of a DPPC Langmuir monolayer with the soluble surfactant SDS was also presented. The presence of an insoluble lipid monolayer at the air-aqueous interface limits the number of soluble surfactant anions that can reside at the aqueous surface. Results indicate that the surfactant species compete for surface sites in the mixed system, with a fraction of the DPPC molecules being replaced by dodecyl sulfate anions at the interface. The soluble surfactant anions influence the conformations of the lipid molecules at the surface. In the presence of SDS, interfacial DPPC molecules are more ordered (have fewer gauche defects) than when residing on a pure water subphase. In addition, the charged surfactant SDS promotes alignment of the interfacial water molecules even in the presence of a DPPC monolayer. These findings are evidence that soluble organic surfactants in the aqueous aerosol core have the potential to influence the surface structure of atmospheric aerosols, which may have important implications in the atmospheric processing of such aerosols.

Finally, the adsorption and uptake of gas-phase alkyl halide and alcohol species by aqueous surfaces was investigated. Using VSFG, both methyl alcohol and butyl alcohol are observed to adsorb to the air-water interface. On the other hand, alkyl halide species (methyl chloride, n-butyl chloride, and n-buytl bromide) are not observed at the aqueous surface during the flow experiments. Because methyl chloride is observed in the bulk aqueous phase using Raman spectroscopy, it is postulated that a convolution of time scale, number density, and disorder prevent detection of the surface species by VSFG. Future studies will investigate possible uptake of the insoluble longer-chain series into

the bulk aqueous phase. Evidence for the uptake of methyl chloride into the bulk phase indicates the possibility for heterogeneous alkyl halide chemistry to occur.

Environmentally relevant interfacial systems are often deeply complex, so a thorough investigation of the heterogeneous chemical and physical processes that occur at such interfaces must start with a careful consideration of the fundamental interactions that govern their structure and composition, as is demonstrated in these experiments.

LIST OF REFERENCES

(1) Finlayson-Pitts, B. J.; Pitts, Jr., J.N. *Chemistry of the Upper and Lower Atmosphere*; Academic Press: New York, 2000.

(2) Knipping, E. M.; Lakin, M. J.; Foster, K. L.; Jungwirth, P.; Tobias, D. J.; Gerber, R. B.; Dabdub, D.; Finlayson-Pitts, B. J. "Experiments and simulations of ion-enhanced interfacial chemistry on aqueous NaCl aerosols." *Science (Washington, D. C.)* **2000**, *288*, 301.

(3) Gill, P. S.; Graedel, T. E.; Weschler, C. J. "Organic films on atmospheric aerosol particles, fog droplets, cloud droplets, raindrops, and snowflakes." *Reviews of Geophysics and Space Physics* **1983**, *21*, 903.

(4) Ellison, G. B.; Tuck, A. F.; Vaida, V. "Atmospheric processing of organic aerosols." *Journal of Geophysical Research, [Atmospheres]* **1999**, *104*, 11633.

(5) Rideal, E. K. "Influence of thin surface films on the evaporation of water." *Journal of Physical Chemistry* **1925**, *29*, 1585.

(6) Langmuir, I.; Schaefer, V. J. "Rates of evaporation of water through compressed monolayers on water." *Journal of the Franklin Institute* **1943**, *235*, 119.

(7) Barnes, G. T. "Permeation through monolayers." *Colloids and Surfaces, A: Physicochemical and Engineering Aspects* **1997**, *126*, 149.

(8) Borden, M. A.; Longo, M. L. "Oxygen Permeability of Fully Condensed Lipid Monolayers." *Journal of Physical Chemistry B* **2004**, *108*, 6009.

(9) Vieceli, J.; Ma, O. L.; Tobias, D. J. "Uptake and Collision Dynamics of Gas Phase Ozone at Unsaturated Organic Interfaces." *Journal of Physical Chemistry A* **2004**, *108*, 5806.

(10) Zhang, H. Z.; Li, Y. Q.; Davidovits, P.; Williams, L. R.; Jayne, J. T.; Kolb, C. E.; Worsnop, D. R. "Uptake of Gas-Phase Species by 1-Octanol. 2. Uptake of Hydrogen Halides and Acetic Acid as a Function of Relative Humidity and Temperature." *Journal of Physical Chemistry A* **2003**, *107*, 6398.

(11) Zhuang, X.; Miranda, P. B.; Kim, D.; Shen, Y. R. "Mapping molecular orientation and conformation at interfaces by surface nonlinear optics." *Physical Review B: Condensed Matter and Materials Physics* **1999**, *59*, 12632.

(12) Hirose, C.; Akamatsu, N.; Domen, K. "Formulas for the analysis of surface sum-frequency generation spectrum by CH stretching modes of methyl and methylene groups." *Journal of Chemical Physics* **1992**, *96*, 997.

(13) Moad, A. J.; Simpson, G. J. "A Unified Treatment of Selection Rules and Symmetry Relations for Sum-Frequency and Second Harmonic Spectroscopies." *Journal of Physical Chemistry B* **2004**, *108*, 3548.

(14) Lambert, A. G.; Davies, P. B.; Neivandt, D. J. "Implementing the theory of sum frequency generation vibrational spectroscopy: a tutorial review." *Applied Spectroscopy Reviews* **2005**, *40*, 103.

(15) Gopalakrishnan, S.; Liu, D.; Allen, H. C.; Kuo, M.; Shultz, M. J. "Vibrational Spectroscopic Studies of Aqueous Interfaces: Salts, Acids, Bases, and Nanodrops." *Chemical Reviews (Washington, DC, United States)* **2006**, *106*, 1155.

(16) Hirose, C.; Akamatsu, N.; Domen, K. *Applied Spectroscopy* **1992**, *46*, 1051.

(17) Atkins, P.W.; Friedman, R.S. *Molecular Quantum Mechanics*, 3rd Ed.; Oxford University Press: USA, 1999.

(18) Hommel, E. L.; Ma, G.; Allen, H. C. "Broadband vibrational sum frequency generation spectroscopy of a liquid surface." *Analytical Science* **2001**, *17*, 1325.

(19) Ma, G.; Allen, H. C. "New insights into lung surfactant monolayers using vibrational sum frequency generation spectroscopy." *Photochemistry and Photobiology* **2006**, *82*, 1517.

(20) Donaldson, D. J.; Vaida, V. "The Influence of Organic Films at the Air-Aqueous Boundary on Atmospheric Processes." *Chemical Reviews (Washington, DC, United States)* **2006**, *106*, 1445.

(21) Tervahattu, H.; Hartonen, K.; Kerminen, V.-M.; Kupiainen, K.; Aarnio, P.; Koskentalo, T.; Tuck, A. F.; Vaida, V. "New evidence of an organic layer on marine aerosols." *Journal of Geophysical Research, [Atmospheres]* **2002**, *107*, AAC 1/1.

(22) Tervahattu, H.; Juhanoja, J.; Kupiainen, K. "Identification of an organic coating on marine aerosol particles by TOF-SIMS." *Journal of Geophysical Research, [Atmospheres]* **2002**, *107*, ACH18/1.

(23) Tervahattu, H.; Juhanoja, J.; Vaida, V.; Tuck, A. F.; Niemi, J. V.; Kupiainen, K.; Kulmala, M.; Vehkamaki, H. "Fatty acids on continental sulfate aerosol particles." *Journal of Geophysical Research, [Atmospheres]* **2005**, *110*, D06207/1.

(24) Voss, L. F. B., M.F.; Beekman, C.P.; Hadad, C.M.; Allen, H.C. *Journal of Geophysical Research* **2006**, in press.

(25) Gaines, J., George L. *Insoluble Monolayers at Liquid-Gas Interfaces*; John Wiley & Sons, Inc.: New York, 1966.

(26) Albrecht, O.; Matsuda, H.; Eguchi, K.; Nakagiri, T. "The dissolution of myristic acid monolayers in water." *Thin Solid Films* **1999**, *338*, 252.

(27) Yang, C. S. C.; Richter, L. J.; Stephenson, J. C.; Briggman, K. A. "In Situ, Vibrationally Resonant Sum Frequency Spectroscopy Study of the Self-Assembly of Dioctadecyl Disulfide on Gold." *Langmuir* **2002**, *18*, 7549.

(28) Ma, G.; Allen, H. C. "DPPC Langmuir Monolayer at the Air-Water Interface: Probing the Tail and Head Groups by Vibrational Sum Frequency Generation Spectroscopy." *Langmuir* **2006**, *22*, 5341.

(29) Holman, J.; Neivandt, D. J.; Davies, P. B. "Nanoscale interference effect in sum frequency generation from Langmuir-Blodgett fatty acid films on hydrophobic gold." *Chemical Physics Letters* **2004**, *386*, 60.

(30) Goncalves da Silva, A. M.; Romao, R. I. S. "Mixed monolayers involving DPPC, DODAB and oleic acid and their interaction with nicotinic acid at the air-water interface." *Chemistry and Physics of Lipids* **2005**, *137*, 62.

(31) Lu, R.; Gan, W.; Wu, B.-h.; Zhang, Z.; Guo, Y.; Wang, H.-f. "C-H Stretching Vibrations of Methyl, Methylene and Methine Groups at the Vapor/Alcohol (n = 1-8) Interfaces." *Journal of Physical Chemistry B* **2005**, *109*, 14118.

(32) Conboy, J. C. Personal communication, 2007.

(33) Goodrich, F. C. Proc. Second Int. Congress Surface Activity; Butterworth: London, 1957, Vol. 1.

(34) Liu, J.; Conboy, J. C. "Structure of a Gel Phase Lipid Bilayer Prepared by the Langmuir-Blodgett/Langmuir-Schaefer Method Characterized by Sum-Frequency Vibrational Spectroscopy." *Langmuir* **2005**, *21*, 9091.

(35) Guyot-Sionnest, P.; Hunt, J. H.; Shen, Y. R. "Sum-frequency vibrational spectroscopy of a Langmuir film: study of molecular orientation of a two-dimensional system." *Physical Review Letters* **1987**, *59*, 1597.

(36) Gragson, D. E.; McCarty, B. M.; Richmond, G. L. "Ordering of Interfacial Water Molecules at the Charged Air/Water Interface Observed by Vibrational Sum Frequency Generation." *Journal of the American Chemical Society* **1997**, *119*, 6144.

(37) Zhang, D.; Gutow, J.; Eisenthal, K. B. "Vibrational Spectra, Orientations, and Phase Transitions in Long-Chain Amphiphiles at the Air/Water Interface: Probing the Head and Tail Groups by Sum Frequency Generation." *Journal of Physical Chemistry* **1994**, *98*, 13729.

(38) Watanabe, N.; Yamamoto, H.; Wada, A.; Domen, K.; Hirose, C.; Ohtake, T.; Mino, N. "Vibrational sum-frequency generation (VSFG) spectra of n-alkyltrichlorosilanes chemisorbed on quartz plate." *Spectrochimica Acta, Part A: Molecular and Biomolecular Spectroscopy* **1994**, *50A*, 1529.

(39) Wang, C.-Y.; Groenzin, H.; Shultz, M. J. "Surface Characterization of Nanoscale TiO2 Film by Sum Frequency Generation Using Methanol as a Molecular Probe." *Journal of Physical Chemistry B* **2004**, *108*, 265.

(40) Adamson, A. W.; Gast, A.P. *Physical Chemistry of Surfaces*, 6th Ed.; John Wiley & Sons, Inc.: New York, 1997.

(41) Meister, A.; Kerth, A.; Blume, A. "Interaction of Sodium Dodecyl Sulfate with Dimyristoyl-sn-glycero-3-phosphocholine Monolayers Studied by Infrared Reflection Absorption Spectroscopy. A New Method for the Determination of Surface Partition Coefficients." *Journal of Physical Chemistry B* **2004**, *108*, 8371.

(42) Prosser, A. J.; Franses, E. I. "Infrared Reflection Absorption Spectroscopy (IRRAS) of Aqueous Nonsurfactant Salts, Ionic Surfactants, and Mixed Ionic Surfactants." *Langmuir* **2002**, *18*, 9234.

(43) Gragson, D. E.; McCarty, B. M.; Richmond, G. L. "Surfactant/Water Interactions at the Air/Water Interface Probed by Vibrational Sum Frequency Generation." *Journal of Physical Chemistry* **1996**, *100*, 14272.

(44) Hauser, H.; Pascher, I.; Pearson, R. H.; Sundell, S. "Preferred conformation and molecular packing of phosphatidylethanolamine and phosphatidylcholine." *Biochimica et Biophysica Acta, Reviews on Biomembranes* **1981**, *650*, 21.

(45) Graedel, T. E.; Keene, W. C. "Tropospheric budget of reactive chlorine." *Global Biogeochemical Cycles* **1995**, *9*, 47.

(46) Butler, J. H. "Atmospheric chemistry: Better budgets for methyl halides?" *Nature (London)* **2000**, *403*, 260.

(47) Keene, W. C.; Khalil, M. A. K.; Erickson, D. J., III; McCulloch, A.; Graedel, T. E.; Lobert, J. M.; Aucott, M. L.; Gong, S. L.; Harper, D. B.; Kleiman, G.; Midgley, P.; Moore, R. M.; Seuzaret, C.; Sturges, W. T.; Benkovitz, C. M.; Koropalov, V.; Barrie, L. A.; Li, Y. F. "Composite global emissions of reactive chlorine from anthropogenic and natural sources: Reactive Chlorine Emissions Inventory." *Journal of Geophysical Research, [Atmospheres]* **1999**, *104*, 8429.

(48) Khalil, M. A. K.; Moore, R. M.; Harper, D. B.; Lobert, J. M.; Erickson, D. J.; Koropalov, V.; Sturges, W. T.; Keene, W. C. "Natural emissions of chlorine-containing gases: Reactive Chlorine Emissions Inventory." *Journal of Geophysical Research, [Atmospheres]* **1999**, *104*, 8333.

(49) Yoshida, Y.; Wang, Y.; Zeng, T.; Yantosca, R. "A three-dimensional global model study of atmospheric methyl chloride budget and distributions." *Journal of Geophysical Research, [Atmospheres]* **2004**, *109*, D24309/1.

(50) Lobert, J. M.; Keene, W. C.; Logan, J. A.; Yevich, R. "Global chlorine emissions from biomass burning: Reactive Chlorine Emissions Inventory." *Journal of Geophysical Research, [Atmospheres]* **1999**, *104*, 8373.

(51) Watling, R.; Harper, D. B. "Chloromethane production by wood-rotting fungi and an estimate of the global flux to the atmosphere." *Mycological Research* **1998**, *102*, 769.

(52) Yokouchi, Y.; Noljiri, Y.; Barrle, L. A.; Toom-Sauntry, D.; Machlda, T.; Inuzuka, Y.; Aklmoto, H.; Li, H. J.; Fujinuma, Y.; Aoki, S. "A strong source of methyl chloride to the atmosphere from tropical coastal land." *Nature (London)* **2000**, *403*, 295.

(53) Yokouchi, Y.; Ikeda, M.; Inuzuka, Y.; Yukawa, T. "Strong emission of methyl chloride from tropical plants." *Nature (London, United Kingdom)* **2002**, *416*, 163.

(54) Bill, M.; Rhew, R. C.; Weiss, R. F.; Goldstein, A. H. "Carbon isotope ratios of methyl bromide and methyl chloride emitted from a coastal salt marsh." *Geophysical Research Letters* **2002**, *29*, 4/1.

(55) Rhew, R. C.; Miller, B. R.; Weiss, R. F. "Natural methyl bromide and methyl chloride emissions from coastal salt marshes." *Nature (London)* **2000**, *403*, 292.

(56) Rasmussen, R. A.; Rasmussen, L. E.; Khalil, M. A. K.; Dalluge, R. W. "Concentration distribution of methyl chloride in the atmosphere." *Journal of Geophysical Research, C: Oceans and Atmospheres* **1980**, *85*, 7350.

(57) Moore, R. M.; Groszko, W.; Niven, S. J. "Ocean-atmosphere exchange of methyl chloride: Results from NW Atlantic and Pacific Ocean studies." *Journal of Geophysical Research, [Oceans]* **1996**, *101*, 28529.

(58) Khalil, M. A. K.; Rasmussen, R. A. "Atmospheric methyl chloride." *Atmospheric Environment* **1999**, *33*, 1305.

(59) Barrie, L. A.; Bottenheim, J. W.; Schnell, R. C.; Crutzen, P. J.; Rasmussen, R. A. "Ozone destruction and photochemical reactions at polar sunrise in the lower Arctic atmosphere." *Nature (London, United Kingdom)* **1988**, *334*, 138.

(60) Bottenheim, J. W.; Gallant, A. G.; Brice, K. A. "Measurements of NOY species and ozone at 82 Deg N latitude." *Geophysical Research Letters* **1986**, *13*, 113.

(61) Anlauf, K. G.; Mickle, R. E.; Trivett, N. B. A. "Measurement of ozone during Polar Sunrise Experiment 1992." *Journal of Geophysical Research, [Atmospheres]* **1994**, *99*, 25.

(62) Oltmans, S. J.; Komhyr, W. D. "Surface ozone distributions and variations from 1973-1984 measurements at the NOAA geophysical monitoring for climatic change baseline observatories." *Journal of Geophysical Research, [Atmospheres]* **1986**, *91*, 5229.

(63) Tarasick, D. W.; Bottenheim, J. W. "Surface ozone depletion episodes in the Arctic and Antarctic from historical ozonesonde records." *Atmospheric Chemistry and Physics [online computer file]* **2002**, *2*, 197.

(64) Foster, K. L.; Plastridge, R. A.; Bottenheim, J. W.; Shepson, P. B.; Finlayson-Pitts, B. J.; Spicer, C. W. "The role of Br2 and BrCl in surface ozone destruction at polar sunrise." *Science (Washington, DC, United States)* **2001**, *291*, 471.

(65) Finlayson-Pitts, B. J. "The Tropospheric Chemistry of Sea Salt: A Molecular-Level View of the Chemistry of NaCl and NaBr." *Chemical Reviews (Washington, DC, United States)* **2003**, *103*, 4801.

(66) Finlayson-Pitts, B. J.; Livingston, F. E.; Berko, H. N. "Ozone destruction and bromine photochemistry at ground level in the Arctic spring." *Nature (London, United Kingdom)* **1990**, *343*, 622.

(67) Tang, T.; McConnell, J. C. "Autocatalytic release of bromine from Arctic snow pack during polar sunrise." *Geophysical Research Letters* **1996**, *23*, 2633.

(68) Domine, F.; Shepson, P. B. "Air-snow interactions and atmospheric chemistry." *Science (Washington, DC, United States)* **2002**, *297*, 1506.

(69) Fan, S. M.; Jacob, D. J. "Surface ozone depletion in Arctic spring sustained by bromine reactions on aerosols." *Nature (London, United Kingdom)* **1992**, *359*, 522.

(70) Mozurkewich, M. "Mechanisms for the release of halogens from sea-salt particles by free radical reactions." *Journal of Geophysical Research, [Atmospheres]* **1995**, *100*, 14.

(71) Rankin, A. M.; Auld, V.; Wolff, E. W. "Frost flowers as a source of fractionated sea salt aerosol in the polar regions." *Geophysical Research Letters* **2000**, *27*, 3469.

(72) Mucha, M.; Frigato, T.; Levering, L. M.; Allen, H. C.; Tobias, D. J.; Dang, L. X.; Jungwirth, P. "Unified Molecular Picture of the Surfaces of Aqueous Acid, Base, and Salt Solutions." *Journal of Physical Chemistry B* **2005**, *109*, 7617.

(73) Koop, T.; Kapilashrami, A.; Molina, L. T.; Molina, M. J. "Phase transitions of sea-salt/water mixtures at low temperatures: Implications for ozone chemistry in the polar marine boundary layer." *Journal of Geophysical Research, [Atmospheres]* **2000**, *105*, 26393.

(74) Swanson, A. L.; Blake, N. J.; Dibb, J. E.; Albert, M. R.; Blake, D. R.; Sherwood Rowland, F. "Photochemically induced production of CH3Br, CH3I, C2H5I, ethene, and propene within surface snow at Summit, Greenland." *Atmospheric Environment* **2002**, *36*, 2671.

(75) Boudries, H.; Bottenheim, J. W.; Guimbaud, C.; Grannas, A. M.; Shepson, P. B.; Houdier, S.; Perrier, S.; Domine, F. "Distribution and trends of oxygenated hydrocarbons in the high Arctic derived from measurements in the atmospheric boundary layer and interstitial snow air during the ALERT2000 field campaign." *Atmospheric Environment* **2002**, *36*, 2573.

(76) Ma, G.; Allen, H. C. "Surface Studies of Aqueous Methanol Solutions by Vibrational Broad Bandwidth Sum Frequency Generation Spectroscopy." *Journal of Physical Chemistry B* **2003**, *107*, 6343.

(77) Stewart, E.; Shields, R. L.; Taylor, R. S. "Molecular Dynamics Simulations of the Liquid/Vapor Interface of Aqueous Ethanol Solutions as a Function of Concentration." *Journal of Physical Chemistry B* **2003**, *107*, 2333.

(78) Taylor, R. S.; Garrett, B. C. "Accommodation of Alcohols by the Liquid/Vapor Interface of Water: Molecular Dynamics Study." *Journal of Physical Chemistry B* **1999**, *103*, 844.

(79) Taylor, R. S.; Ray, D.; Garrett, B. C. "Understanding the mechanism for the mass accommodation of ethanol by a water droplet." *Journal of Physical Chemistry B* **1997**, *101*, 5473.

(80) Tarek, M.; Tobias, D. J.; Klein, M. L. "Molecular dynamics investigation of an ethanol-water solution." *Physica A: Statistical and Theoretical Physics (Amsterdam)* **1996**, *231*, 117.

(81) Socrates, G. *Infrared and Raman Characteristic Group Frequencies-Tables and Charts*, 3rd Ed.; John Wiley & Sons, Ltd.: New York, 2001.

(82) Jayne, J. T.; Duan, S. X.; Davidovits, P.; Worsnop, D. R.; Zahniser, M. S.; Kolb, C. E. "Uptake of gas-phase alcohol and organic acid molecules by water surfaces." *Journal of Physical Chemistry* **1991**, *95*, 6329.

(83) Fournier, F.; Dubost, H.; Carrez, S.; Zheng, W.; Bourguignon, B. "Interaction of coadsorbed CH3Cl and D2O layers on Pd(111) studied by sum frequency generation." *Journal of Chemical Physics* **2005**, *123*, 184705/1.

(84) Physical Constants of Organic Compounds. In *CRC Handbook of Chemistry and Physics, Internet Version 2007*, 87th Ed.; Lide, D. R., Ed.; Taylor and Francis: Boca Raton, FL, 2007.